THE ASTROPHYSICAL JOURNAL SUPPLEMENT SERIES, 121:483–513, April 1999

LONG-TERM SCINTILLATION STUDIES OF PULSARS. I. OBSERVATIONS AND BASIC RESULTS

N. D. RAMESH BHAT, A. PRAMESH RAO, AND YASHWANT GUPTA
National Centre for Radio Astrophysics, Tata Institute of Fundamental Research, Post Bag 3, Ganeshkhind, Pune 411 007, India
Received 1998 April 20; accepted 1998 November 2

ABSTRACT

We report long-term scintillation observations of 18 pulsars in the dispersion measure range 3–35 pc cm^{-3} carried out from 1993 January to 1995 August using the Ooty Radio Telescope at 327 MHz. These observations were made with the aim of studying refractive effects in pulsar scintillation and obtaining reliable estimates of diffractive and refractive scintillation properties. Dynamic scintillation spectra of pulsars were regularly monitored at 10–90 epochs spanning 100–1000 days. Significant changes are observed in the dynamic spectra over timescales as short as a few days. Large-amplitude fluctuations are observed in quantities such as decorrelation bandwidth, scintillation timescale, drift rate, and flux density. Several pulsars show organized features, such as drifting bands in a highly pronounced manner. For some pulsars, gradual and systematic variations are seen in the drift rate of patterns that undergo several sign reversals during the observing time spans. Anomalous behavior, such as persistent drifts lasting over many months, is seen for PSRs B0834+06 and B1919+21. Four pulsars were studied for 2–4 well-separated observing sessions, each lasting over $\sim$100 days. In some cases, significant variations are seen in the average scintillation properties and/or flux densities between successive observing sessions. From our data, we have been able to obtain more accurate and reliable estimates of scintillation properties and flux densities than those from the earlier observations by averaging out the fluctuations due to refractive scintillation effects. These measurements are used to derive parameters such as the strength of scattering and scintillation speeds. The scintillation speed estimates are found to be reasonably good indicators of proper-motion speeds of pulsars. The present measurements are compared with earlier measurements and the long-term stability of scintillation properties and flux densities is discussed.

Subject headings: ISM: general — ISM: structure — pulsars: general — scattering

1. INTRODUCTION

There are several classes of pulsar intensity variations seen at radio wavelengths. The large-amplitude, broadband, pulse-to-pulse variations seen for most pulsars are thought to be intrinsic to the pulsar emission mechanism. When averaged over many pulses to smooth out these variations, pulsar intensities show fluctuations occurring over timescales ranging from minutes to hours, which are explained in terms of propagation of radio waves through the irregular interstellar plasma (Scheuer 1968; Rickett 1969). Random variations of electron densities in the interstellar medium (ISM) give rise to phase perturbations, leading to scattering of radio waves. As they propagate, the scattered waves interfere with each other, causing large variations of amplitude with frequency and position. The relative motion between the pulsar, observer, and the density irregularities translates the spatial amplitude variations into temporal variations at a given position, leading to a typical timescale of intensity fading, called the scintillation timescale. Other observable consequences of this phenomenon are broadening of pulse profiles and angular broadening of compact radio sources at low frequencies. Observations of pulsar dynamic spectra (e.g., Roberts & Ables 1982; Smith & Wright 1985), which are records of intensity variations in the time-frequency plane, reveal that such intensity variations are fairly narrowband—decorrelation bandwidths $\sim$100 kHz to a few MHz—and exhibit modulations as large as 100%. This phenomenon, which has become known as diffractive interstellar scintillation (DISS), has been extensively studied since the early days of pulsar observations and is quite well understood (see Rickett 1977 for a review). DISS studies have been used for probing the structure of electron density inhomogeneities in the ISM (e.g., Cordes, Weisberg, & Boriakoff 1985; Armstrong, Rickett, & Spangler 1995) and to estimate pulsar velocities (e.g., Cordes 1986).

The discovery of long-term ($\sim$days to months) flux variations (e.g., Cole, Hesse, & Page 1970; Huguenin, Taylor, & Helfand 1973) and the subsequent correlation of these timescales with dispersion measure (DM; Sieber 1982) led to the recognition of a second class of propagation effects (Rickett, Coles, & Bourgois 1984), which has become known as refractive interstellar scintillation (RISS). In RISS, flux variations arise because of focusing and defocusing of the scattered radiation by electron density irregularities that are large compared to the Fresnel scale. These modulations are fairly broadband in nature. Refraction through the large-scale density structures also produces the systematic "drifting patterns" that are often seen in pulsar dynamic spectra (e.g., Smith & Wright 1985; Hewish 1980). RISS is also thought to be responsible for the occasional occurrences of quasi-periodic intensity modulations in the dynamic spectra (e.g., Wolszczan & Cordes 1987; Hewish, Wolszczan, & Graham 1985). RISS is also the preferred explanation for other observed phenomena, like slow flux variability at meter wavelengths (e.g., Rickett 1986), centimeter wavelength "flickering," and discrete propagation events (e.g., Fiedler et al. 1987) with compact extragalactic radio (EGR) sources (see Rickett 1990 for a review). Besides flux modulations, RISS is also thought to produce slow modulations of decorrelation bandwidth and scintillation timescale. It has been suggested that the large irregularities responsible for RISS are part of the same spectrum of irregularities that give rise to DISS (Rickett et al. 1984), and studies of both phenomena provide us information on the spectrum over a very large range of spatial scales (several

orders of magnitude). While it is generally considered to be of a power-law form over the spatial scales of interest for interstellar scintillation (ISS), the exact form of the spectrum, especially the slope, cutoffs, and above all the validity of a simple power-law description still remain to be well understood (see Narayan 1988; Rickett 1990; Armstrong et al. 1995).

On the theoretical front, several researchers have addressed the problem of DISS and RISS in terms of small-scale ($\sim 10^6$–10^8 m) and large-scale ($\sim 10^{10}$–10^{12} m) electron density fluctuations producing two distinct regimes of scintillations (Rickett et al. 1984; Cordes, Pidwerbetsky, & Lovelace 1986; Romani, Narayan, & Blandford 1986). Besides predicting the long-term flux variations that characterize RISS, these models make predictions about the nature and levels of fluctuations for observables such as decorrelation bandwidth, scintillation timescale, and the drift rates of intensity patterns in pulsar dynamic spectra. In the case of power-law models for the density irregularities, the refractive effects are expected to depend on the slope of the spectrum. For example, the magnitude of the fluctuations of all the above parameters is predicted to increase substantially with the slope (Romani et al. 1986; Blandford & Narayan 1985).

On the observational front, significant work has been done to measure the long-term flux modulations of several pulsars (Stinebring & Condon 1990; Kaspi & Stinebring 1992; Gupta, Rickett, & Coles 1993; LaBrecque, Rankin, & Cordes 1994). The results show that, for several pulsars, the measured flux modulation indices are larger than those predicted by the simple Kolmogorov model, indicating that the underlying density spectrum may be more complicated. Not much is known about the timescales and the magnitudes of the flux variation due to RISS and about other scintillation variables like decorrelation bandwidth and scintillation timescale. A recent study of the long-term variations in pulsar dynamic spectra (Gupta, Rickett, & Lyne 1994) has shown that the properties of scintillation patterns of several pulsars vary considerably with time, and, to a first order, these variations were found to be consistent with expectations from RISS. However, several discrepancies with the predictions of a Kolmogorov model were also observed in these data. Observations also show occurrences of unusual scattering effects such as episodes of multiple imaging and extreme scattering events (ESE), which are thought to be due to refraction by discrete structures in the ISM (e.g., Cordes & Wolszczan 1986; Fiedler et al. 1987). Most ESEs have been with EGR sources (Fiedler et al. 1994), and the only pulsar that is reported to have shown ESEs (in the form of unusual flux variations and timing perturbations) is PSR B1937+21 (Cognard et al. 1993; Lestrade, Rickett, & Cognard 1998). More recently, there have been a couple of attempts to test the quantitative predictions of theories, and for two pulsars (PSRs B0329+54 and B1937+214) the correlations between the fluctuations of scintillation observables were found to be consistent with the predictions (Lestrade, Cognard, & Biraud 1995; Stinebring, Faison, & McKinnon 1996). However, the results are not conclusive, and there is a need for more observations of this kind, which is one of the motivations for the observations described in this paper.

The fluctuations of the flux and the DISS parameters caused by refractive scintillation lead to unreliable estimates of flux densities, scattering properties, and pulsar velocities if obtained from only a few epochs of observations. In order to get reliable estimates of these quantities, the refractive fluctuations need to be averaged out by taking measurements at a large number of epochs spanning several refractive timescales. The timescales of the fluctuations due to RISS, largely determined by the strength of scattering and the pulsar velocity, can range from a few days (for nearby pulsars at meter wavelengths) to several years (in the case of distant pulsars at longer wavelengths). Most scintillation measurements made earlier (Roberts & Ables 1982; Cordes et al. 1985; Smith & Wright 1985; Cordes 1986) could not take into consideration such effects (probably because of limited observing time), and the scattering properties derived from such measurements are prone to errors due to refractive scintillation. For example, in the published literature, estimates of decorrelation bandwidth and time by different observers differ by factors of 3–5. A second motivation of the present work is to examine whether such discrepancies are attributable to RISS and to make a better determination of the scintillation parameters.

In order to investigate refractive scintillation effects and to obtain reliable estimates of scintillation properties of nearby pulsars, we undertook long-term systematic scintillation observations of 18 pulsars using the Ooty Radio Telescope (ORT) during 1993–1995. Our observations and measurements of the scintillation properties are presented in this paper (referred to as Paper I). In Paper II (Refractive effects and the spectrum of plasma density fluctuations), we use our results to constrain the electron density spectrum in the local ISM. In Paper III (Testing theoretical models of refractive scintillation), we compare our results with existing theoretical models of RISS. In an earlier paper (Bhat, Gupta, & Rao 1998), we have used our improved estimates of the average scintillation properties of several local pulsars to show that the distribution of scattering material in the local ISM is not homogeneous and that it supports the presence of the Local bubble.

The layout for the rest of this paper is as follows: Our observations are described in § 2. A description of the data analysis methods is given in § 3, where we also present results on the diffractive and refractive scintillation properties. We discuss the reliability of the present measurements in § 4, where we also compare the present measurements with those from earlier observations and address the issue of long-term stability of scintillation properties and pulsar fluxes; § 5 gives a summary of our main conclusions from this work.

2. OBSERVATIONS

2.1. *Instrument and Data Acquisition*

The observations were made using the ORT, which is an equatorially mounted 530 × 30 m parabolic cylinder operating at 327 MHz (Swarup et al. 1971). The telescope has an effective collecting area of 8000 m^2 and a system temperature of 150° K; it is sensitive to linearly polarized radiation with an electric field in the north-south plane. It has $9\frac{1}{2}$ hr of hour angle coverage and a declination coverage from $-55°$ to $+55°$. The ORT is a phased array, with 1056 dipoles at its feed, which was upgraded recently giving considerable improvement in sensitivity and stability (Selvanayagam et al. 1993). With the current sensitivity, a signal-to-noise ratio of 25 can be achieved for a 1 Jy source, for 1 s integration, and over a bandwidth of 4 MHz. The

signals from the dipole array are combined to form two signals from the north and south halves of the telescope. These are input to a 1 bit correlation spectrometer (Subramanian 1989) to yield the cross power spectrum of the signals from the two halves. For our experiment, pulsar data were taken over a bandwidth of 9 MHz centered at 327 MHz. The data were obtained such that there are 64 frequency channels in the cross spectrum spanning the observing bandwidth, yielding a frequency resolution ≈ 140 kHz.

Pulsar data were acquired with a sampling interval of 6 ms. The data were recorded both on the pulse and on part of the off-pulse regions. The gated on-pulse and off-pulse regions were synchronously averaged in the correlation domain over a specified number of pulse periods and then recorded for off-line analysis. A continuum source at a declination close to that of the pulsar being studied was observed for calibration. The data from the calibrator were acquired for typical durations of 5 minutes, and an equal stretch of data were acquired by pointing the telescope to a cold region of the sky. The calibration observations were generally made before starting the pulsar observations. A suitable calibrator was chosen for each pulsar so as to eliminate any possible bias in the flux calibration. The data from several calibrators taken on a given observing day were also used to monitor the stability of the telescope gain over the observing periods.

2.2. *Sample Selection*

Our sample selection was made with the twofold aim of (1) studying diffractive and refractive scintillations and (2) obtaining reliable estimates of scattering properties of nearby (distance $\lesssim 1$ kpc) pulsars. It was largely determined by our preliminary calculations of expected scintillation parameters based on the earlier scintillation measurements available from the literature and the instrumental constraints. For the pulsars that were known at the time of our observations with DM < 40 pc cm^{-3} and within the sky coverage of ORT, the expected values of decorrelation widths in frequency ($\Delta\nu_{\rm iss}$) and in time ($\tau_{\rm iss}$) were calculated from published results, assuming the scaling laws for a Kolmogorov density spectrum ($\Delta\nu_{\rm iss} \propto f_{\rm obs}^{4.4}$, $\tau_{\rm iss} \propto f_{\rm obs}^{1.2}$). Pulsars whose scintillation patterns could be studied with a frequency resolution of 140 kHz over a 9 MHz band were selected. The temporal resolution required to resolve the scintillation patterns in time is typically 10 s at 327 MHz. In order to have a sufficient signal-to-noise ratio with this integration time, we included in our sample only those pulsars whose flux at 327 MHz was greater than 25 mJy ($S_{400} \lesssim 20$ mJy). The minimum integration time with the correlation spectrometer being 6 ms, we eliminated from our sample short-period pulsars (period $\lesssim 100$ ms). We also left out pulsars that are known to show intrinsic intensity variations (such as nulling) over timescales comparable to that of ISS. Pulsars for which no prior scintillation measurements were available but that satisfied our selection criteria of DM, flux, and period were retained in the sample. The final sample consisted of 18 pulsars in a DM range 5–35 pc cm^{-3} and are listed in Table 1 along with relevant observational details. Pulsar names are listed in column (2) and their DMs in column (3). Distance estimates adopted in our calculations (col. [4]) are based on the electron density distribution given by Taylor & Cordes (1993), except for PSR B0823+26, for which we use the independent distance estimate available from parallax measurements (Gwinn et al. 1986). The period of observation and the total number of epochs of observation are given in columns (5) and (6). The instrumental resolutions in frequency and time used for each pulsar are listed in columns (7) and (8). The pulsar sample spans the DM range fairly uniformly and therefore allows us to study variations of diffractive and refractive

TABLE 1

THE PULSAR SAMPLE AND THE OBSERVING PARAMETERS

Number (1)	Pulsar (2)	DM (pc cm^{-3}) (3)	D (pc) (4)	Period of Observation (5)	$N_{\rm ep}$ (6)	$\Delta f_{\rm ch}$ (kHz) (7)	Δt (s) (8)	$\tau_{r,\rm exp}$[a] (days) (9)
1	PSR B0329+54	26.8	1430	1995 Apr–Jul	14	140.6	7.15	39.7
2	PSR B0628−28	34.4	2140	1993 Oct–1994 Jan	17	140.6	12.44	14.6
3	PSR B0823+26	19.5	380[b]	1993 Mar–1994 Jan	31	140.6[c]	13.27	5.5
4	PSR B0834+06	12.9	720	1993 Jan–1995 Jul	93	140.6[c]	12.74	5.2
5	PSR B0919+06	27.2	2970[d]	1994 Mar–Jun	19	140.6	21.53	12.6
6	PSR B1133+16	4.8	270	1993 Feb–1995 Jul	59	140.6[c]	11.88	1.4
7	PSR B1237+25	9.3	560	1993 Oct–1994 Jan	9	140.6	13.82	2.2
8	PSR B1508+55	19.6	1930	1995 Apr–Jul	9	140.6	14.79[e]	15.1
9	PSR B1540−06	18.5	1160	1995 Apr–Jul	12	140.6	14.18	12.0
10	PSR B1604−00	10.7	590	1995 Apr–Jul	10	140.6	21.09	13.4
11	PSR B1747−46[f]	21.7	1080	1995 Apr–Jul	12	140.6	14.85[e]	...
12	PSR B1919+21	12.4	660	1993 Mar–1994 Jan	63	140.6[c]	13.37	6.5
13	PSR B1929+10	3.2	170	1994 Mar–Jun	9	140.6	11.33	2.7
14	PSR B2016+28	14.2	1100	1993 Oct–1994 Jan	20	140.6	13.95	77.4
15	PSR B2020+28	24.6	1300	1994 Mar–Jun	15	140.6	17.20[e]	22.5
16	PSR B2045−16	11.5	640	1993 Oct–1994 Jan	35	140.6	19.62	1.4
17	PSR B2310+42[f]	17.3	960	1995 Apr–Jul	10	140.6	17.47	...
18	PSR B2327−20[f]	8.4	490	1994 Mar–Jun	18	140.6	32.87	...

[a] Estimates are based on the measurements from Cordes 1986.
[b] The distance estimates are from parallax measurements (Gwinn et al. 1986).
[c] Part of the data were taken with $\Delta f_{ch} = 281.20$ kHz.
[d] Lower limit on the distance estimate.
[e] Part of the data were taken with larger Δt (twice the value given here).
[f] Scintillation measurements are not reported so far for these pulsars.

properties over a range of DM, distance, and strength of scattering.

2.3. *Observing Strategy*

Each pulsar was observed at several epochs spanning many months. For accurate estimates of diffractive scintillation parameters at each epoch, observations need to be made over a time duration much larger than the characteristic timescales ($t_{obs} \gg \tau_{iss}$) and over bandwidths much larger than characteristic frequency widths ($B_{obs} \gg \Delta\nu_{iss}$) of patterns. Since we had a fixed observing bandwidth of 9 MHz, pulsars that were expected to have large decorrelation bandwidths ($\Delta\nu_{iss} \sim 1$ MHz) or decorrelation times ($\tau_{iss} \sim 1000$ s) were observed for longer durations (typically $\sim$2–3 hr) in order to ensure sufficiently large number of *scintles* needed to obtain good ensemble averages of scintillation properties. Pulsars with relatively shorter decorrelation widths either in time or in frequency were observed for shorter durations of about 1–2 hr. For refractive scintillation studies, dynamic spectra need to be monitored regularly for time spans much longer than their typical refractive timescales, with several observations within the timescale. We estimated the expected values of refractive timescales ($\tau_{r,exp}$) using the diffractive timescales available in the literature in order to decide the initial observing strategies for individual pulsars. The values of $\tau_{r,exp}$ are given in column (9) of Table 1. Since these timescales range from days to weeks, observations were made over time spans of about $\sim$100 days to ensure a sufficiently large number of refractive cycles of fluctuations. The final strategies in terms of number of epochs and their separations were largely influenced by the results from our own early observations.

Our final data are from four observing sessions during 1993 January–1995 August, with each session lasting over a period of 100–150 days. In every observing session, six to eight pulsars were regularly monitored for their dynamic spectra. The number of epochs of observations (N_{ep}) has a wide range, from 9 to 93, the reasons for which are as follows: 10 pulsars, with $N_{ep} \gtrsim 20$, were primarily observed for studying the refractive effects in dynamic spectra, while for the remaining nine, our basic aim was to obtain reliable estimates of scintillation properties for the purpose of studying the local ISM. Four pulsars were reobserved in multiple sessions because of interesting scintillation properties observed during the initial sessions. In Table 2, column (3) gives the number of observing sessions (N_{sess}) for each pulsar. In columns (4)–(7), the break up of number of epochs for each session is given, where the quantity shown in brackets is the time span of observation in days. The total time span of observation ($T_{sp,max}$) is given in column (8). Pulsars PSR B0823+26 and PSR B1919+21 were observed over two sessions, the former because of unusual flux variations that were seen and the latter because of the presence of persistent drift slopes. The basic interest in the case of PSR B1133+16, which was observed for three sessions, was the dramatic changes observed in the characteristics of its scintillation patterns. Pulsar PSR B0834+06 was observed for the largest time span of observation (four sessions) to study persistent drift slopes seen in its dynamic spectra. The data of these four pulsars also proved to be useful in investigating the long-term stability of both diffractive and refractive scintillation properties over timescales much longer than their refractive timescales.

3. DATA ANALYSIS AND RESULTS

3.1. *Data Reduction Procedure*

3.1.1. *The Dynamic Scintillation Spectra*

To calibrate the pulsar data, data were acquired on both a nearby calibration source and a cold region of the sky. These data were used to estimate the gain of the telescope at the declination of the pulsar and to determine the bandpass of the correlation receiver. For most observations, frequency channels beyond the 3 dB range (about 7 MHz) were not used. The off-source data were examined for bad channels and line interference, which were flagged for the pulsar data.

Pulsar data from the correlation spectrometer were edited for occurrences of instrumental malfunctions. The data were calibrated for the telescope gain as well as gain variations across the observing band. The data were dedispersed and examined for any systematic pulse drifts due to instrumental effects, which were corrected if detected. An integrated profile was obtained by averaging the pulsar data over the entire observing duration and over the usable range of the observing bandwidth. The on-pulse region was identified using a 5 σ (where σ is the rms of the off-pulse region) threshold criterion above the mean off-pulse level. The mean off-level was subtracted from the corresponding on-pulse region, and the dynamic spectrum was obtained by integrating this over the on-pulse time bins. A similar spectrum was created for the average value of the off-pulse region, which was used to detect regions of dynamic spectra corrupted by external interference. The data were checked for both narrowband and broadband spurious signals, lasting over very short durations to the entire observing time, and the corrupted data regions were given zero weights in the further analysis. The fraction of the data rejected in this manner seldom exceeds a few percent. The pulsar flux density (F), averaged over the bandwidth and

TABLE 2

PULSARS OBSERVED FOR MULTIPLE SESSIONS

			Number of Epochs of Observation per Session (N_{ep})				
Number (1)	Pulsar (2)	N_{sess} (3)	Session I (1993 Jan–May) (4)	Session II (1993 Oct–1994 Jan) (5)	Session III (1994 Feb–Jun) (6)	Session IV (1995 Apr–Jul) (7)	$T_{sp,max}$ (days) (8)
1.....	PSR B0823+26	2	12 (66)	21 (87)	...	...	305
2.....	PSR B0834+06	4	27 (120)	18 (74)	21 (78)	27 (100)	935
3.....	PSR B1133+16	3	6 (19)	...	25 (90)	27 (95)	928
4.....	PSR B1919+21	2	15 (59)	48 (87)	...	...	305

duration of the observations, and the intensity modulation index (m_d) were computed from the on-pulse dynamic spectra.

3.1.2. *The Computation of Autocovariance Functions*

In order to quantify the average characteristics of scintillation patterns at any epoch, we make use of the two-dimensional autocovariance function (2D ACF), which was computed for frequency lags up to half the observing bandwidth and for time lags up to half the observing time. The function was corrected for the effect of receiver noise fluctuations and the residual, intrinsic pulse-to-pulse fluctuations, which remain uncorrelated and appear as a "ridgelike" feature at zero time lag in the 2D ACF. We computed a weight function for the 2D ACF that represents the uncertainties in the ACF values and is given by

$$\omega_d(\nu, \tau) = \sigma_n \left[\frac{N(\nu = 0, \tau = 0)}{N(\nu, \tau)} \right]^{0.5}, \quad (1)$$

where ν and τ are the frequency and time lags and $N(\nu, \tau)$ is the number of data pairs averaged in computing the ACF value at (ν, τ). The quantity σ_n represents the rms noise in the ACF at $\nu = 0$ and $\tau = 0$, and it was computed from the region of the ACF where interstellar features are absent. This weight function was used while fitting the 2D ACF with suitable functions.

3.2. *Description of Data*

Sample dynamic spectra are shown in Figures 1*a*–1*h* and 3*a*–3*m*. These spectra have been selected to illustrate the general characteristics of pulsar scintillation as well as to highlight the observed variations from pulsar to pulsar and epoch to epoch. In Figures 1*a*–1*h*, there are a number of panels, each displaying the spectrum at a given epoch. Multiple panels are shown mainly to highlight the changing form of dynamic spectra with time. The observing durations are typically 2–3 hr, but often the displays have been restricted to shorter durations ($\sim$100 minutes), because this is sufficient to illustrate the basic features. Most data have resolutions of 140 kHz in frequency and 10 s in time. The date of observation is indicated at the top right corner of each panel, and the mean flux density for each epoch is shown at the top left corner. In the gray-scale representation of the intensity, darker regions correspond to higher intensity values and lighter regions to lower values. The display saturates to black at 4 times the mean intensity, and white regions are usually at about 20% of the mean. There are bright intensity regions, usually known as scintles, which are resolvable when their widths in frequency and time are larger than the instrumental resolution. A typical spectrum consists of a large number of such scintles of varying intensity, shape, and widths. Such random, deep modulations of intensities, occurring over narrow frequency ranges and short time intervals, are general features of all spectra. Various time-dependent instrumental problems, as well as external broadband interference, that have been identified and blanked out in our data reduction process appear as vertical white regions that are distinguishable from regions of real flux fading by their sharp boundaries. The horizontal white strips seen in some of the spectra [for example, in Figs. 1*b* and 1*g*, i.e., pulsars PSR B0834+06(I) and PSR B1919+21(I)] are regions of the data corrupted by narrowband interferences. However, as seen in the figures, only a very small fraction of the data is corrupted by such spurious signals; therefore, this does not affect the estimation of the scintillation parameters.

Sample ACFs of some selected pulsars are displayed in Figures 2*a*–2*c* to illustrate the general characteristics of ACFs and to highlight the special features seen with some of the pulsars. Each figure has a number of panels representing the ACF of the dynamic spectrum obtained on the observing day indicated at the top of the panel. The displays are restricted to much smaller ranges in frequency and time lags than the maximum lag ranges for which the ACFs have been computed.

The sample data shown here (Figs. 1–3) illustrate the diversity seen in the pulsar dynamic spectra. The properties of patterns, such as their sizes and shapes in the time-frequency plane, vary significantly from pulsar to pulsar. The widths of intensity patterns vary from $\sim$100 s (e.g., PSR B0823+26, PSR B0919+06, and PSR B2045−16) to as large as $\sim$1000 s (e.g., PSR B1604−00 and PSR B2016+28) in time and from $\sim$100 kHz (e.g., PSR B0329+54, PSR B1540−06, and PSR B2310+42) to several MHz (e.g., PSR B1133+16, PSR B1237+25, and PSR B1929+10) in frequency. Organized drifting of scintles in the frequency-time plane is seen in the dynamic spectra of several pulsars. The data of PSR B0834+06, PSR B1133+16, PSR B1919+21, and PSR B2045−16 are some of the best examples with prominent drifting patterns.

The changing form of dynamic spectra with epoch is a common feature for all pulsars and significant variations are seen over timescales as short as a few days. The property is better illustrated through the plots of ACFs, whose widths and orientations show significant variations from epoch to epoch. Significant variations are also present in the average flux densities of pulsars. Generally, at a given epoch of observation most of the intensity patterns appear with quite similar orientations in the time-frequency plane. But there are slow variations in the magnitudes of tilts from epoch to epoch, which is seen as a changing nature of elongations of the ACFs. For many pulsars, pattern tilts undergo sign reversals over timescales of the order of several days. Pulsars PSR B0823+26 and PSR B0919+06 are good examples, showing such systematic variations of pattern slopes along with sign reversals.

Systematic slope variations and sign reversals are found to be common for most of the pulsars observed. There are, however, some pulsars whose data are characterized by very few or even an absence of sign reversals of pattern slopes over the observing time spans (typically $\sim$100 days). Pulsars PSR B0834+06 and PSR B1919+21 are the best examples of such "persistent drift slopes." PSR B1919+21 is a unique case, where in addition to the usual intensity decorrelations there are deep intensity modulations lasting over very short timescales (roughly 1 minute). This broadband phenomenon is found to be a stable feature of this pulsar over the entire observing session. Another special pulsar is PSR B1133+16, which shows remarkable changes in the nature of the dynamic spectrum between its successive observing sessions. On 1994 April 30 this pulsar shows periodic intensity modulations in the dynamic spectrum.

In the rest of this section, we briefly describe the observed properties of some of the pulsars that show typical behavior and some with anomalous scintillation properties. This is followed by a brief summary of the general characteristics of the remaining pulsars.

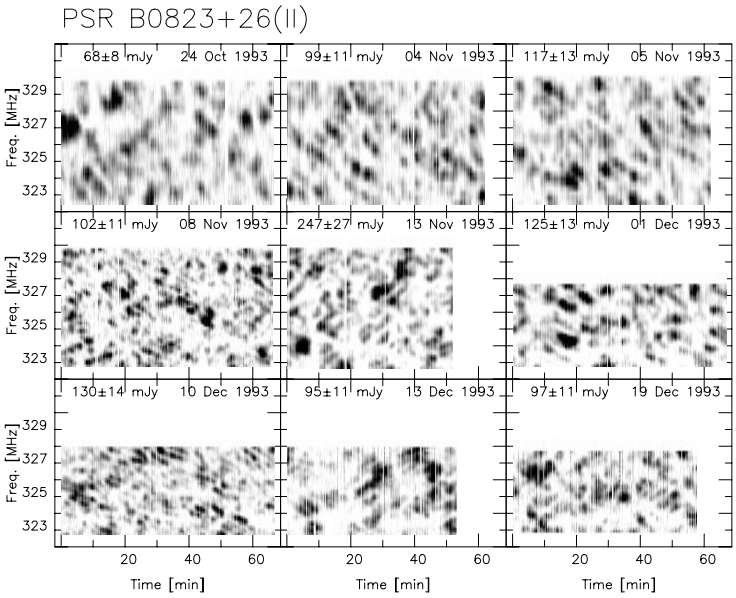

FIG. 1*a*

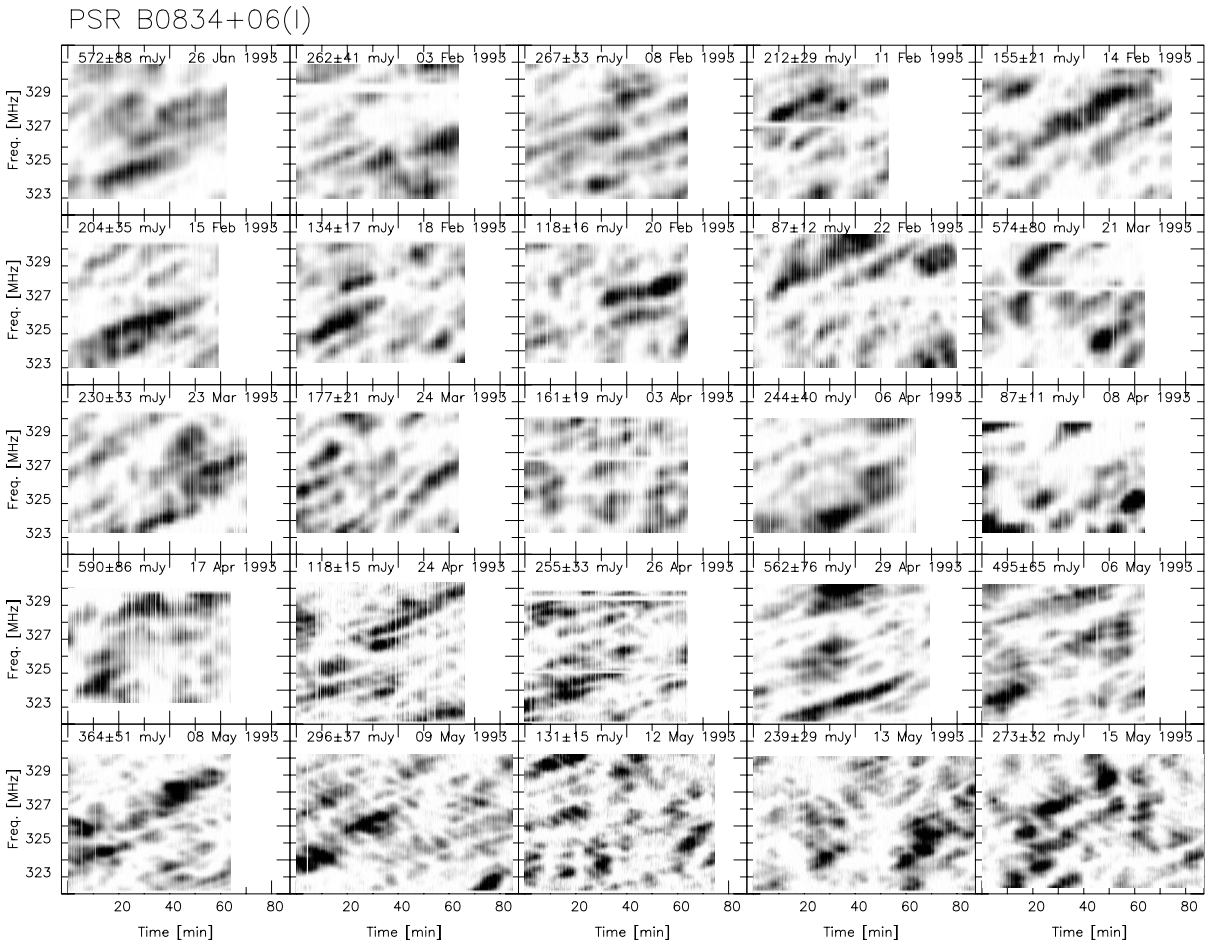

FIG. 1*b*

FIG. 1.—Sample dynamic spectra of selected pulsars shown as a gray-scale plot of intensity vs. time and frequency. The darker regions represent higher intensity values. The white regions correspond to 20% of the mean intensity, and the black regions correspond to four times the mean intensity; in between, the intensity values are linearly represented by the gray scale. The average flux density at each epoch of observation is given at the upper left corner of each panel, and the observing day is indicated at the upper right corner. (*a*) PSR B0823 + 26 at nine epochs spanning 57 days during 1993 October–December; (*b*) PSR B0834 + 06 at 25 epochs spanning 110 days during 1993 January–May; (*c*) PSR B0834 + 06 at 23 epochs spanning 100 days during 1995 April–July; (*d*) PSR B0919 + 06 at nine epochs spanning 35 days during 1994 March–June; (*e*) PSR B1133 + 16 at 16 epochs spanning 65 days during 1994 March–May; (*f*) PSR B1133 + 16 at 16 epochs spanning 92 days during 1995 April–July; (*g*) PSR B1919 + 21 at nine epochs spanning 23 days during 1993 April–May; and (*h*) PSR B2045 − 16 at nine epochs spanning 40 days during 1993 December–1994 January.

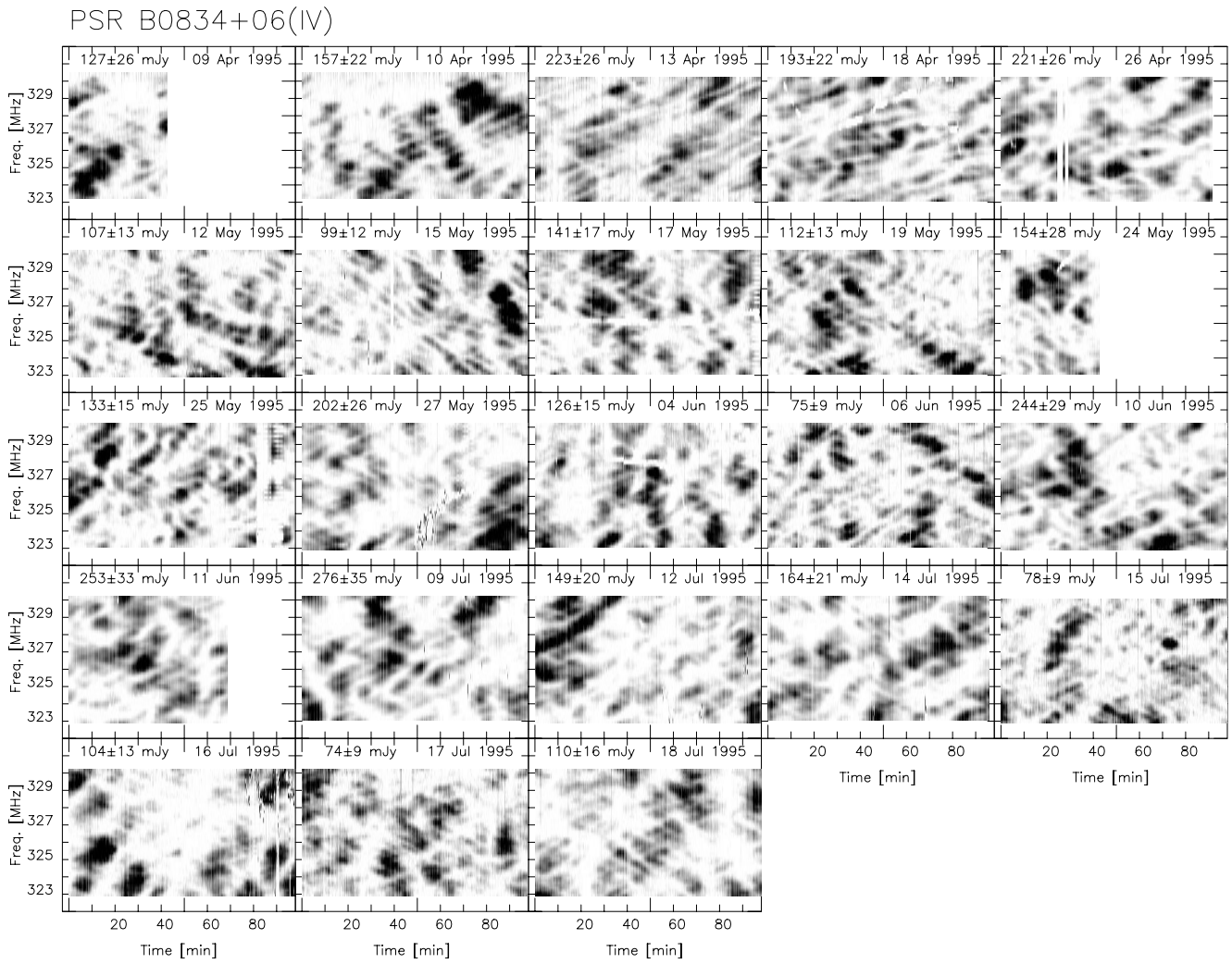
PSR B0834+06(IV)
127±26 mJy 09 Apr 1995
157±22 mJy 10 Apr 1995
223±26 mJy 13 Apr 1995
193±22 mJy 18 Apr 1995
221±26 mJy 26 Apr 1995
107±13 mJy 12 May 1995
99±12 mJy 15 May 1995
141±17 mJy 17 May 1995
112±13 mJy 19 May 1995
154±28 mJy 24 May 1995
133±15 mJy 25 May 1995
202±26 mJy 27 May 1995
126±15 mJy 04 Jun 1995
75±9 mJy 06 Jun 1995
244±29 mJy 10 Jun 1995
253±33 mJy 11 Jun 1995
276±35 mJy 09 Jul 1995
149±20 mJy 12 Jul 1995
164±21 mJy 14 Jul 1995
78±9 mJy 15 Jul 1995
104±13 mJy 16 Jul 1995
74±9 mJy 17 Jul 1995
110±16 mJy 18 Jul 1995
Freq. [MHz]
323
325
327
329
20 40 60 80
Time [min]

FIG. 1*c*

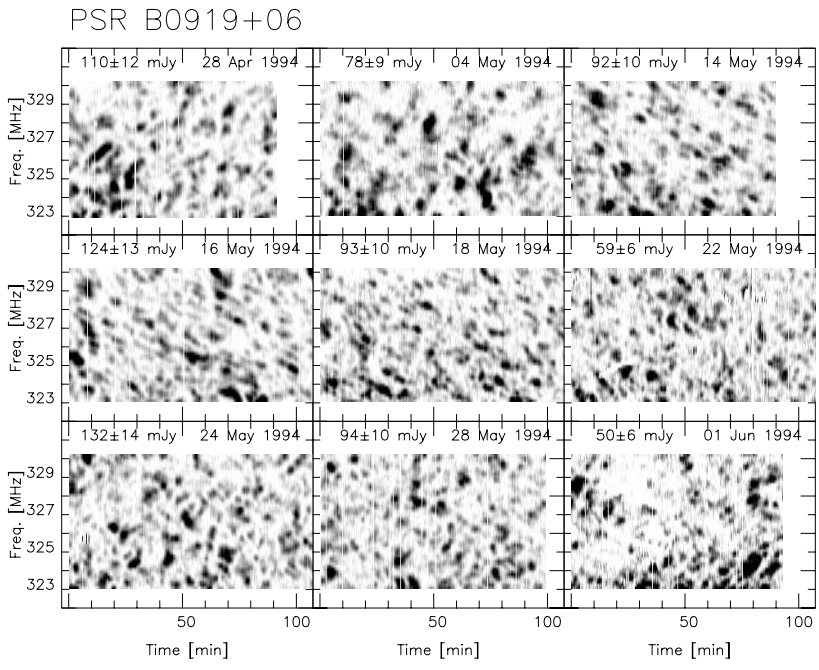
PSR B0919+06
110±12 mJy 28 Apr 1994
78±9 mJy 04 May 1994
92±10 mJy 14 May 1994
124±13 mJy 16 May 1994
93±10 mJy 18 May 1994
59±6 mJy 22 May 1994
132±14 mJy 24 May 1994
94±10 mJy 28 May 1994
50±6 mJy 01 Jun 1994
Freq. [MHz]
323
325
327
329
50 100
Time [min]

FIG. 1*d*

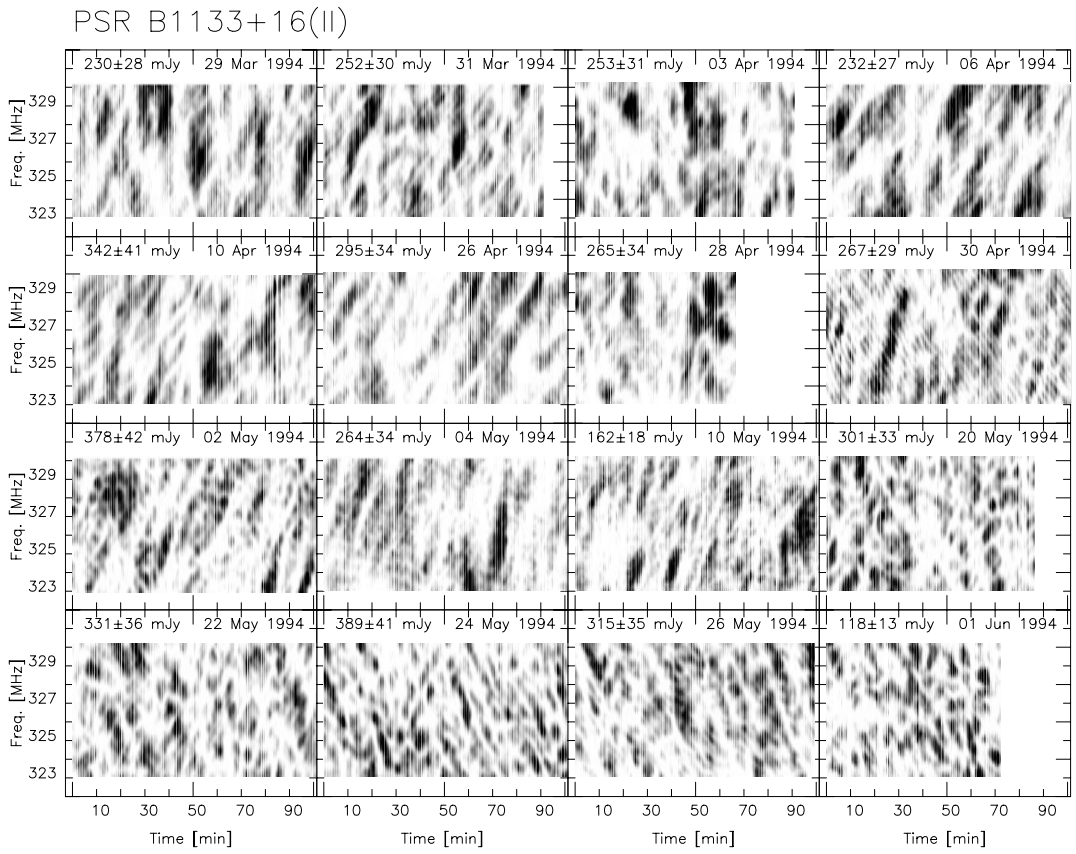
PSR B1133+16(II)
230±28 mJy 29 Mar 1994
252±30 mJy 31 Mar 1994
253±31 mJy 03 Apr 1994
232±27 mJy 06 Apr 1994
342±41 mJy 10 Apr 1994
295±34 mJy 26 Apr 1994
265±34 mJy 28 Apr 1994
267±29 mJy 30 Apr 1994
378±42 mJy 02 May 1994
264±34 mJy 04 May 1994
162±18 mJy 10 May 1994
301±33 mJy 20 May 1994
331±36 mJy 22 May 1994
389±41 mJy 24 May 1994
315±35 mJy 26 May 1994
118±13 mJy 01 Jun 1994
Freq. [MHz]
329
327
325
323
10 30 50 70 90
Time [min]

FIG. 1*e*

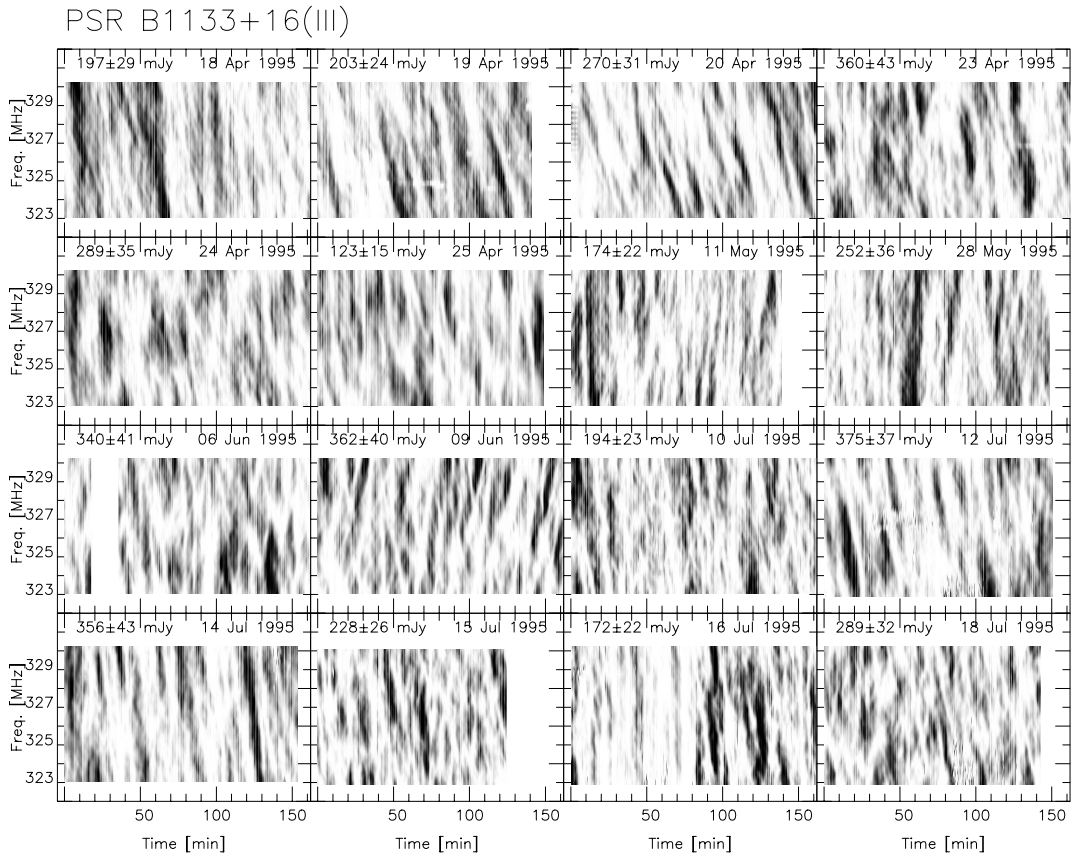
PSR B1133+16(III)
197±29 mJy 18 Apr 1995
203±24 mJy 19 Apr 1995
270±31 mJy 20 Apr 1995
360±43 mJy 23 Apr 1995
289±35 mJy 24 Apr 1995
123±15 mJy 25 Apr 1995
174±22 mJy 11 May 1995
252±36 mJy 28 May 1995
340±41 mJy 06 Jun 1995
362±40 mJy 09 Jun 1995
194±23 mJy 10 Jul 1995
375±37 mJy 12 Jul 1995
356±43 mJy 14 Jul 1995
228±26 mJy 15 Jul 1995
172±22 mJy 16 Jul 1995
289±32 mJy 18 Jul 1995
Freq. [MHz]
329
327
325
323
50 100 150
Time [min]

FIG. 1*f*

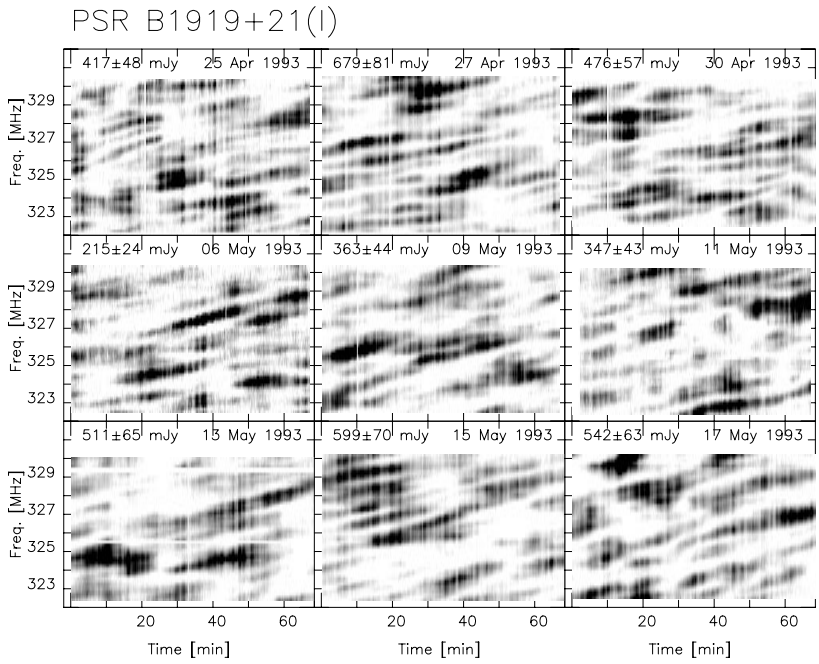

FIG. 1*g*

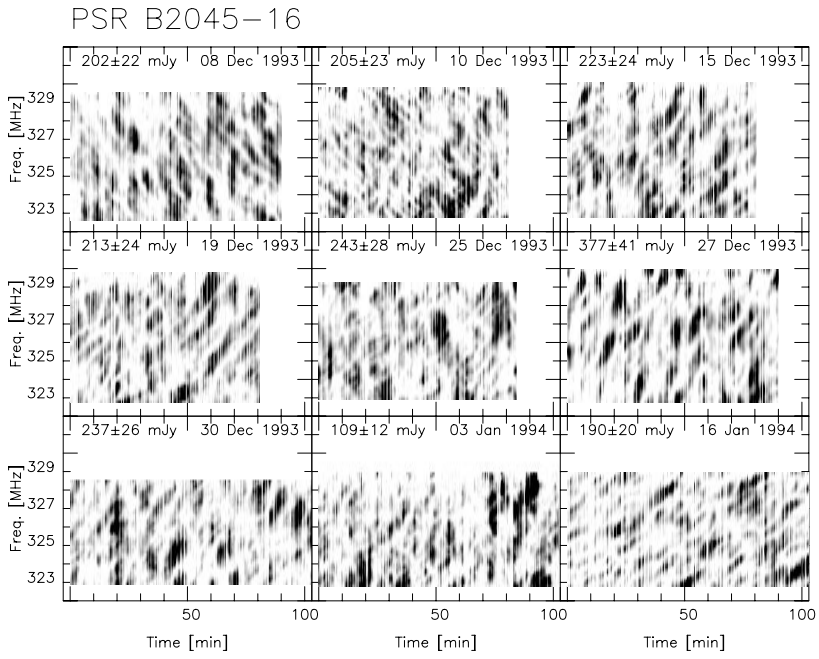

FIG. 1*h*

3.2.1. *PSR B0823+26*

Sample data of this pulsar are shown in Figure 1*a*, which has nine dynamic spectra spanning a period of 57 days from the second observing session (1993 October–1994 January), and in Figure 2*a*, which shows nine selected ACFs spanning 54 days from the first observing session (1993 March–May). These data illustrate a number of basic observable effects due to diffractive and refractive scintillations. The intensity scintillation patterns arising from rapid intensity modulations in time and frequency are clearly seen. The patterns decorrelate over a few 100 kHz in frequency and $\sim$100 s in time for this pulsar. Often the patterns appear with preferred orientations in the time-frequency plane, and on a given day most of them exhibit slopes of the same sign, either positive or negative. The sloping features in the dynamic spectra produce tilted contours in the ACFs. In addition, there are fine variations of sizes and shapes of patterns from day to day, along with significant variations in the average flux density. The property is better illustrated in Figure 2*a*, where ACFs at various epochs differ in terms of their sizes and elongations. A systematic slope reversal can be seen in the six ACFs starting from 1993 April 26.

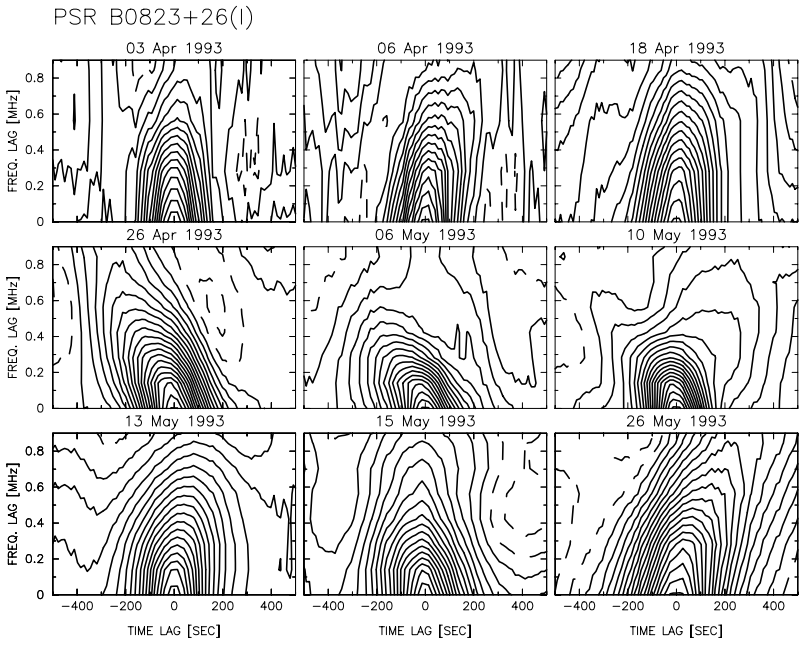

FIG. 2*a*

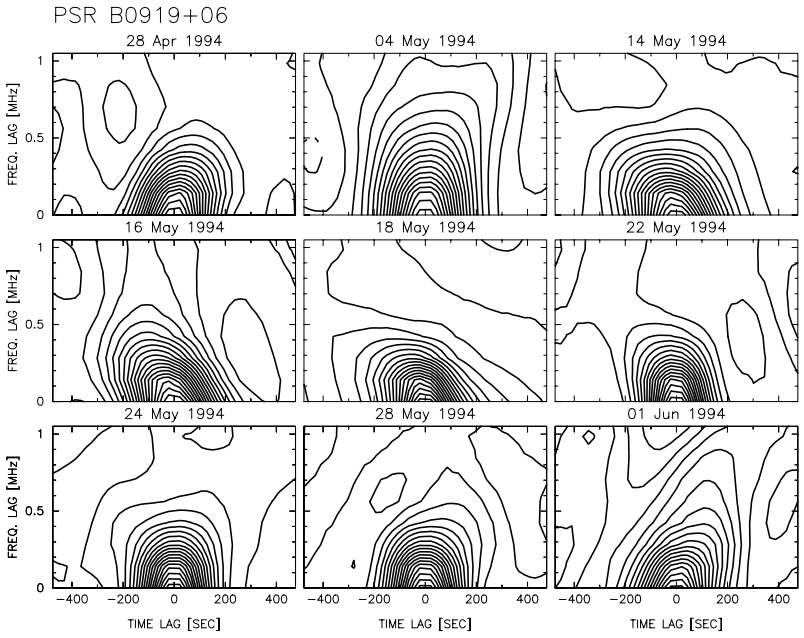

FIG. 2*b*

FIG. 2.—Contour plots of 2D ACF of dynamic spectra shown for three pulsars. There are 20 contours over the range zero to unity; successive contours are separated by an interval 0.05, and dashed contours represent negative values. The date of observation is indicated at the top of each panel. (*a*) PSR B0823 + 26 at nine epochs of observations spanning 54 days during 1993 April–May; (*b*) PSR B0919 + 06 at nine epochs of observations spanning 35 days during 1994 April–June; and (*c*) PSR B1919 + 21 at 25 epochs of observations spanning 87 days during 1993 October–1994 January.

3.2.2. *PSR B0834+06*

Figure 1*b* show the dynamic spectra for this pulsar at 25 epochs spanning a period of 110 days, taken from the first observing session (1993 January–May). A similar data set (at 23 epochs spanning 100 days) from the final observing session (1995 April–July) is displayed in Figure 1*c*. These data have been selected to illustrate a number of special properties seen with this pulsar. Drifting patterns are highly pronounced in the dynamic spectra of this pulsar (Fig. 1*b*). Scintles are much broader than that of PSR B0823+26, with typical widths of $\sim$500 kHz in frequency and $\sim$400 s in time. The variable nature of dynamic spectra is also much better pronounced here. In the data taken from the first session (Fig. 1*b*), patterns appear with slopes of the same sign for all the epochs and do not show any reversal in between. Such persistent drifting features are also seen in the data from the next two observing sessions, 1993 October–1994 January and 1994 February–June. However, quite dramatic changes are noticed in the data taken during the final session, 1995 April–July (Fig. 1*c*), in which there

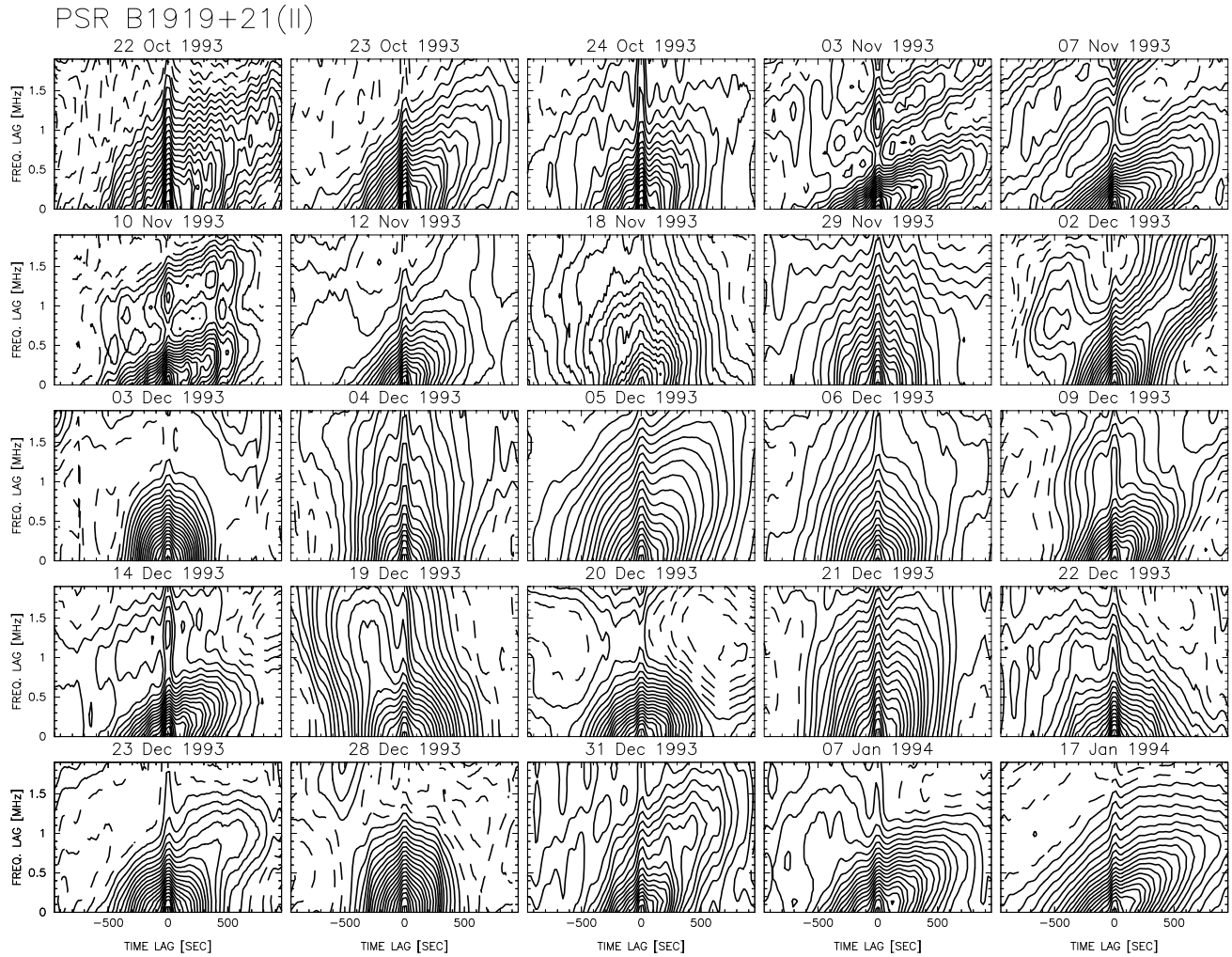

FIG. 2*c*

are several occasions of slope reversals. In addition, there are a few examples of spectra with "dual slopes" (e.g., 1995 June 10).

3.2.3. *PSR B0919+06*

Selected dynamic spectra and ACFs of this pulsar are shown in Figures 1*d* and 2*b*, where the data at nine epochs spanning a period of 35 days are displayed. The behavior of this pulsar is quite similar to that of PSR B0823+26. Intensity patterns fade over a few 100 kHz in frequency and ~100 s in time, and the widths vary significantly between successive epochs of observation. Gradual and systematic variations in the slopes of the patterns are highly pronounced here. In fact, the orientation of the major angle of the ACF reverses its sign twice—from 1994 April 28 to May 14 and then again from 1994 May 16 to June 1. In some ACFs there is evidence for a dual slope, where the orientation is different for the higher and lower contours: data on May 4, 14, and 24 are good examples. Such behaviors can be expected during the transition periods of drift reversals, which is clearly substantiated by the dynamic spectra. This means, for this pulsar, pattern slopes seem to undergo a sign reversal typically once in 20 days.

3.2.4. *PSR B1133+16*

Another special pulsar is PSR B1133+16, which shows remarkable changes in properties of its dynamic spectra from one observing session to another. The pulsar was observed for three well-separated sessions over a 3 yr period. Figure 1*e* displays the dynamic spectra of this pulsar from the observations during March 1994–June 1994. A similar data set from the third session (1995 April–July) is shown in Figure 1*f*. Each figure consists of data from 16 epochs of observations. Data shown in Figures 1*e* and 1*f* span 65 and 92 days, respectively. A typical dynamic spectrum from the initial observing session (1993 February) is shown in Figure 3*c*, which is characterized by intensity patterns fading over approximately a few 100 kHz in frequency and over approximately 100 s in time. In contrast, dynamic spectra taken during the second session (Fig. 1*e*), in particular those from the first half of the session, show patterns that fade over much broader ranges in frequency (~1 MHz) and in time (~200 s). The spectrum on 1994 April 30 shows clear evidence of periodic intensity modulations in the frequency-time plane, known as "interstellar fringes," which result from multiple imaging caused by refraction in the ISM (e.g., Wolszczan & Cordes 1987). It may be mentioned that such imaging events were reported earlier for this pulsar by Hewish et al. (1985) and Cordes & Wolszczan (1986). After this episode of fringes, the pulsar appears to return to the initial mode seen in session I, with intensity patterns fading over ~a few 100 kHz in frequency and over ~100 s in time. This mode of scintillation spectrum prevails

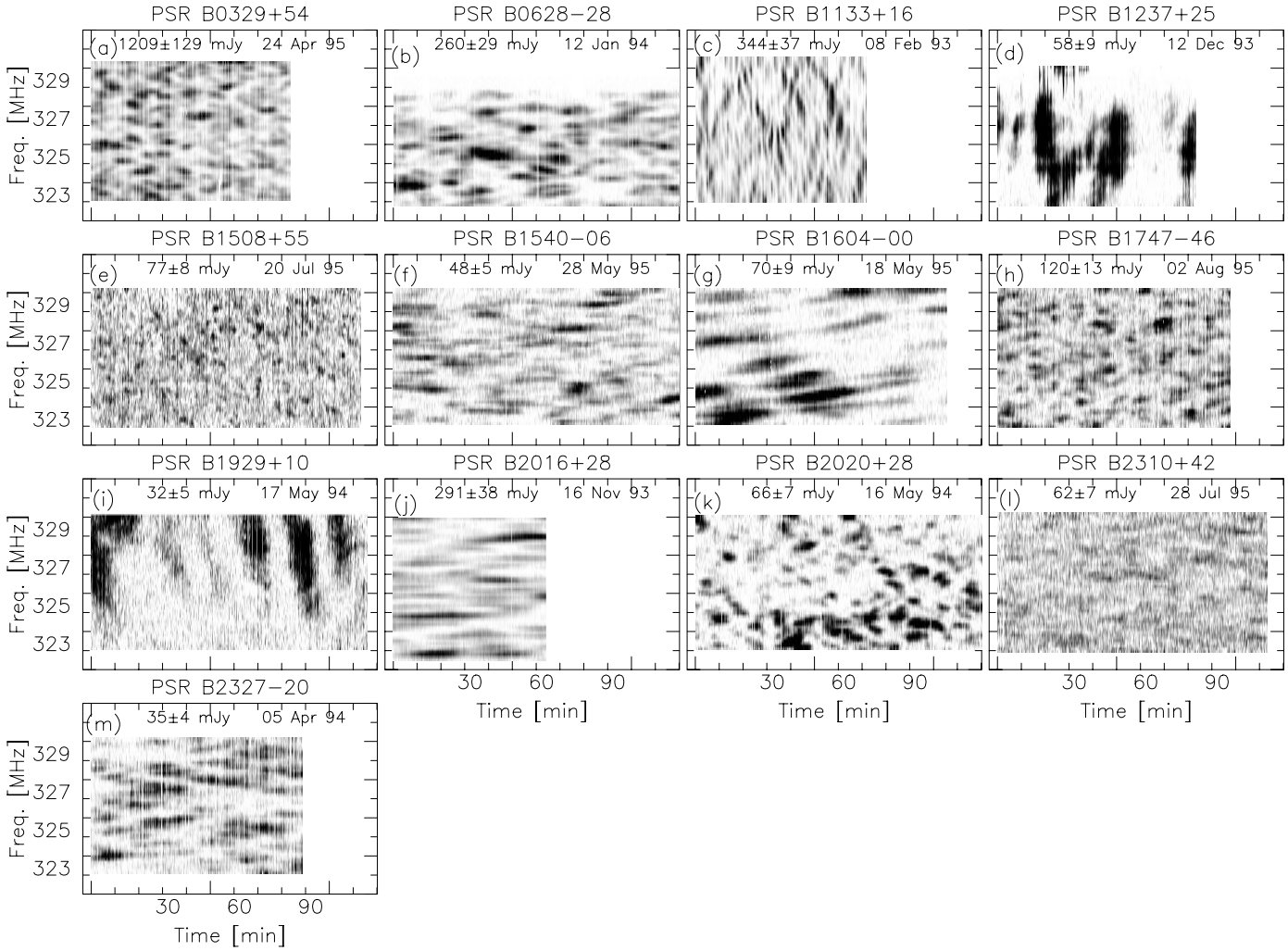

FIG. 3.—Typical dynamic spectra of 13 pulsars shown to illustrate their general characteristics. The name of the pulsar is given at the top of each panel. The average flux density is given at the upper left corner, and the date of observation is given at the upper right corner of each panel. The nature of gray-scale representation is similar to Fig. 1 except for the intensity levels corresponding to the white and black regions. The white and black correspond to 20% and four times the mean intensity, respectively, for PSRs B0628−28, B1237+25, B1604−00, B1929+10, B2020+28, and B2327−20. They correspond to 30% and four times the mean for PSRs B1133+16, B1540−06, and B2016+28; 30% and thrice the mean for PSRs B0329+54 and B1747−46; and 40% and thrice the mean for PSRs B1508+55 and B2310+42.

until the last observing day of the session (1994 June 1). Surprisingly, the dynamic spectra data obtained from the subsequent observing session (Fig. 1*f*) are markedly different from the earlier data, showing intensity patterns fading over much broader ranges in frequency (∼a few MHz), which is similar to the characteristics of the first half of session II and sometimes seem to be broader than the observing bandwidth itself. The pulsar thus seems to exhibit drastic changes in the nature of its dynamic spectrum on timescales ∼1 yr. Behavior of this kind is not seen for any other pulsar that was followed up for multiple observing sessions.

3.2.5. *PSR B1919+21*

Selected dynamic spectra of PSR B1919+21 from the first observing session (1993 March–May) are shown in Figure 1*g*, and Figure 2*c* shows selected ACFs from the follow-up session (1993 October–1994 January). The spectra in Figure 1*g* are from nine observations spanning 23 days, and the ACFs displayed in Figure 2*c* are for 25 observations over a period of 87 days. These data have been selected to highlight some of the special properties seen with this pulsar. The dynamic spectra appear to be quite similar to that of PSR B0834+06 shown in Figure 1*b*, but substantial variations are seen in size and shape of ACF over a time interval as short as 1–2 days.

A noticeable property seen in the dynamic spectra of this pulsar is fine, deep modulations of intensity patterns, which are invariably broadband and last over ∼100 s in time. The property is unique to this pulsar and is a stable feature in the data from both the observing sessions. These intensity modulations produce a narrow ridge in the ACF at zero time lag (see Fig. 2*c*). Sometimes, this effect also leads to fine corrugations of the ACF along the time axis (see, e.g., ACFs on 1993 October 22 and November 29). Because of its broadband nature and persistence over entire duration of observation, we believe that these modulations are intrinsic to the pulsar and are not a scintillation phenomenon. Thus the ACFs of this pulsar are more complex than those of the rest of the pulsars.

Drifting patterns are highly pronounced in the dynamic spectra of this pulsar (Fig. 1*g*), as is the persistent nature of

drift slopes. The data from the follow-up observations (Fig. 2*c*) during 1993 October–1994 January also show persistent tilts in the ACF. There seems to be occasional instances of reversals of drift slopes, but the overall appearance of the data are more like that of persistent drifts. No further observations were made, and hence no information is available on how long the persistent drifting features last for this pulsar.

3.2.6. *PSR B2045−16*

Sample dynamic spectra of this pulsar are displayed in Figure 1*h*, which consists of observations at nine epochs spanning a period of 40 days. The pattern drifts are quite prominent as in PSR B0834+06 and PSR B1133+16 and show large variations and a number of reversals of slope over a period of 3 months. In contrast with the data discussed so far, the intensity patterns of this pulsar show random occurrences of broadband intensity fluctuations lasting for a few time samples ($\sim$10 s), thereby giving rise to white vertical strips in its dynamic spectra. Broadband features of this kind are attributable to an insufficient averaging of pulsar's intrinsic intensity variations due to the presence of additional phenomena like nulling.

3.2.7. *Summary of the Remaining Pulsars*

The data of PSR B2020+28 (typical spectrum is shown in Fig. 3*k*) show a behavior quite similar to that of PSR B0919+06 and PSR B0823+26. The data of pulsars PSR B0628−28 and PSR B2327−20 are also found to be quite similar to that of PSR B0823+26 and PSR B0919+06, except that patterns fade over much longer durations, typically $\sim$500 s. Typical spectra of these pulsars are shown in Figures 3*b* and 3*m*, respectively. There are frequent, broadband striations in the spectrum of PSR B2327−20, which are presumably due to residual intrinsic intensity variations. Typical spectra of PSR B1604−00 and PSR B2016+28 are shown in Figures 3*g* and 3*j*, where the intensity patterns fade over much longer durations in time, typically $\sim$1000 s. The sloping patterns are not quite noticeable in the spectra of PSR B2016+28. In contrast, PSR B1604−00 shows prominent drift slopes, which vary systematically and show a sign reversal in between. The spectra of this pulsar are rather poorly sampled, and there are only 10 epochs of observations over a time span of 94 days. Figures 3*d* and 3*i* show typical spectra of pulsars PSR B1237+25 and PSR B1929+10. For these pulsars, patterns are much broader in frequency and fade over a range $\sim$1 MHz. Often their spectra are characterized by a few bright scintles that dominate over others and last for $\sim$1000 s; these are followed by long fading over similar timescales. The presence of bright scintles also cause apparent intensity modulations that are somewhat greater than 100%. In the case of pulsars PSR B0329+54, PSR B1540−06, and PSR B2310+42, typical spectra of which are shown in Figures 3*a*, 3*f*, and 3*l*, respectively, the intensity patterns fade over a very narrow frequency range, sometimes as small as $\sim$100 kHz, which is close to our spectral resolution limit. The patterns are thus significantly smoothed in frequency because of the instrumental resolution, and this smoothing effect reduces apparent intensity modulations to somewhat below 100%. The spectra of pulsars PSR B1508+55, PSR B1747−46, and PSR B2310+42 (Figs. 3*e*, 3*h*, and 3*l*, respectively) are characterized by poor signal-to-noise ratio because of a significant reduction in the telescope gain at high declinations.

3.3. *Estimation of Scintillation Properties*

3.3.1. *ACF Fitting and Estimation of Scintillation Parameters*

The 2D ACF can be characterized by its widths along the frequency lag and time lag axes and its orientation in the frequency lag–time lag plane. The parameters corresponding to these widths are the decorrelation bandwidth, ν_d, defined as the half-power width along the frequency lag axis at $\tau = 0$ and the scintillation time, τ_d, defined as the e^{-1} width along the time lag axis at $\nu = 0$. The 2D ACF is fitted with a two-dimensional elliptical Gaussian function (see Gupta et al. 1994 for justification) of the following form:

$$\rho_k^m(\nu, \tau) = C_0 \exp\left[-(C_1 \nu^2 + C_2 \nu\tau + C_3 \tau^2)\right] . \quad (2)$$

The amplitude of the Gaussian function, C_0, is unity, since the ACF itself is normalized to unity. In the fitting algorithm, the deviations between the ACF and the model Gaussian are weighted by their uncertainties given by the weight function, ω_d, as described in equation (1). This weighting scheme accounts for the measurement uncertainties in the ACF values due to finite data stretch and does not take care of the "scintle-lumpiness" effect arising because of the finite number of scintles (this is addressed later in this section). The model Gaussian parameters, C_1, C_2, and C_3, are estimated by a χ^2 minimization procedure. The scintillation parameters ν_d and τ_d are obtained from these fitted parameters as

$$\nu_d = \left(\frac{\ln 2}{C_1}\right)^{0.5}, \quad \tau_d = \left(\frac{1}{C_3}\right)^{0.5} . \quad (3)$$

The decorrelation widths ν_d and τ_d obtained in this manner are corrected for smearing due to finite instrumental resolutions in frequency and in time using a quadrature subtraction scheme. Barring a few exceptions, such as ν_d measurements of pulsars PSR B1540−06 and PSR B2310+42, this correction is not significant for our measurements.

To characterize the drifting features in the dynamic spectra (or, equivalently, the tilt or orientation of the fitted Gaussian ρ_k^m), two issues need to be addressed. The first is the choice of an appropriate quantity for describing the effect. Usually the sloping features have been characterized by the frequency drift rate, measured as $d\nu/dt$ (Hewish 1980; Smith & Wright 1985). More recently, the inverse of this quantity, i.e., $dt/d\nu$, has been suggested as a more appropriate choice (Spangler 1988; Rickett 1990; Gupta et al. 1994), since it has a more meaningful connection with theory. The inverse of this quantity, $dt/d\nu$, is proportional to the refractive scattering angle θ_r and will have the same statistical properties: zero mean random variable, in the simplest case. We therefore prefer to use $dt/d\nu$ in place of $d\nu/dt$ in characterizing drift slopes.

The second issue concerns the correct method of estimating $dt/d\nu$. At first sight, it may appear that the slope of the major axis of the ellipse fitted to the ACF is a good measure of $dt/d\nu$. However, this is not true, since the ellipticity and hence the slope of the major axis depend on the plotted scale and can give results that are not meaningful when the major axis happens to be aligned along one of the axes. The basic effect of refraction due to a linear phase gradient is not a tilting of the entire pattern but rather a "shear" resulting from the frequency-dependent displacements of patterns in the observing plane. Therefore, in the quantity $dt/d\nu$, dt

should refer to the time interval corresponding to the differential displacement of intensity patterns separated in frequency by dv. The proper measure of dt/dv would be the slope of the line joining the points on the ellipse with the highest correlation at a given frequency offset. This definition is similar to that suggested by Gupta et al. (1994). It results in a zero drift slope in the absence of sloping patterns and is also free from the ambiguity of determining the major axis. In terms of the fitted Gaussian parameters, this slope can be expressed as

$$\frac{dt}{dv} = -\left(\frac{C_2}{2C_3}\right). \tag{4}$$

The uncertainties in C_1, C_2, and C_3 due to the Gaussian model fitting are obtained from the χ^2 analysis and translated into corresponding uncertainties in v_d, τ_d, and dt/dv; they are referred to as $\sigma_{\rm mod}$. We also take into account the statistical uncertainties in the scintillation parameters arising because of the finite number of scintles, given by

$$\sigma_{\rm est} = \left[f_d \left(\frac{B_{\rm obs}\, t_{\rm obs}}{v_d\, \tau_d} \right) \right]^{-0.5}, \tag{5}$$

where $\sigma_{\rm est}$ is the fractional error and f_d is the filling fraction for number of scintles, which is assumed to be 0.5 in our calculations. This is just a moderate value and may overestimate the number of scintles (hence underestimate $\sigma_{\rm est}$) if typical separation between the scintles is much larger than their sizes. For the parameters v_d, τ_d, and dt/dv, errors from the Gaussian fitting ($\sigma_{\rm mod}$) are added in quadrature with the statistical errors to get their final uncertainties. The typical values of $\sigma_{\rm mod}$ and $\sigma_{\rm est}$ correspond to errors of 10% and 5%, respectively.

Similar statistical errors are also applicable for the measurements of pulsar flux densities and intensity modulation indices, which are directly obtained from the dynamic spectra. The intensity modulation index, which is known as the diffractive scintillation index, m_d, is usually found to be close to unity, within the measurement uncertainties. Moreover, the measured fluctuations of m_d are found to be comparable to the uncertainties in m_d values, and hence m_d can be treated as a stable quantity. The observed 100% intensity modulations are in accordance with the strong scintillation expected for pulsars at meter wavelengths. However, there are a few exceptions (such as PSRs B1237+25 and B1929+10) with significant deviations of indices from unity, and they are found to result from dominance of a few bright scintles. Occasionally, indices greater than unity are seen when a few bright scintles dominate the dynamic spectrum. However, no pulsar shows any systematic, large variations of m_d.

3.3.2. *Time Series and Average Values of Scintillation Parameters*

The results from the analysis are presented in the form of time series of four quantities: the three scintillation parameters v_d, τ_d and dt/dv, and average flux density (F). These are shown in Figures 4*a*–4*x*, where results for each session of every pulsar are shown as a separate panel, divided into four subpanels showing variations of the four quantities. In each figure, day 1 corresponds to the starting day of observation. When the pulsar was observed for more than one session, the results are shown separately, since we find that the successive sessions show significant difference in the scintillation properties. Thus there are four panels for PSR B0834+06 and two each for PSR B0823+26, PSR B1133+16, and PSR B1919+21 (see Table 2 for details). The uncertainties of individual measurements are estimated as described in the previous section. The length of the error bar represents ± 1 σ uncertainty in the measurement. The data points are joined with dotted lines merely to illustrate the general trends seen in the variations of the quantities. We now use these time series to derive the average properties characterizing the diffractive and refractive scintillations for each pulsar.

The parameters v_d and τ_d form two basic observables of diffractive scintillation that are measurable from our data. The present observations show that they vary significantly with time, which is presumably because of refractive effects. We discuss the details of the modulation characteristics in a later section. The important point here is that scintillation measurements from only a few observations would lead to erroneous conclusions about average scattering parameters. Most earlier measurements in the literature could not take into consideration such effects, probably because of limited observing time. It is necessary to average out these fluctuations in order to get reliable estimates of the quantities. Our observations were made over time spans much longer than the expected timescales of fluctuations, and we were able to obtain many more scintillation measurements on each pulsar in our program. Thus the data allow us to reduce the errors due to refractive scintillation effects, as a result of which we are able to estimate DISS parameters more robustly than previous attempts. The average values thus obtained, $\langle v_d \rangle$ and $\langle \tau_d \rangle$, are listed in columns (2) and (3) of Table 3. It may be mentioned that our data span may be insufficient to yield stable ISS parameters for pulsars that show persistent drifting features lasting many months.

The third parameter dt/dv is basically related to refractive scattering. Nevertheless, we briefly describe it here, because the quantity is measured from the dynamic spectra, which is due to DISS. Like v_d and τ_d, the drift slopes of intensity patterns also show significant variations with time. The theoretical expectation is that these slopes should vary randomly about a zero mean over refractive timescales. In general, most pulsars show this basic property where the slopes change their magnitudes and show frequent sign reversals. However, PSR B0834+06 and PSR B1919+21 seem to be exceptions; the former does not show sign reversals in the first three sessions, and the latter shows quite similar property, although there are a few epochs of opposite drift slopes. Thus, excepting a few pulsars, the mean value of the drift rate $\langle dt/dv \rangle$ (given in the col. [4] of Table 3) is zero within the estimation errors.

3.3.3. *The Global ACF Computation*

Here we describe an alternative method that gives more reliable estimates of average values of v_d, τ_d, and dt/dv than obtained by averaging the time series. The method makes use of a weighted average 2D ACF, which we refer to as the global 2D ACF (GACF). It is computed from the ACFs at all the epochs of observation for a given pulsar using the definition

$$\rho_g(\nu, \tau) = \frac{\sum_{k=1}^{k=N'_{\rm ep}} \varpi_k(\nu, \tau)\rho_k(\nu, \tau)}{\sum_{k=1}^{k=N'_{\rm ep}} \varpi_k(\nu, \tau)}, \tag{6}$$

where ρ_k is the ACF of dynamic spectrum at the kth epoch, $N'_{\rm ep}$ is the number of observations made with identical resolutions in time and frequency, and ϖ_k is the weight function for the GACF, which is simply the number of data

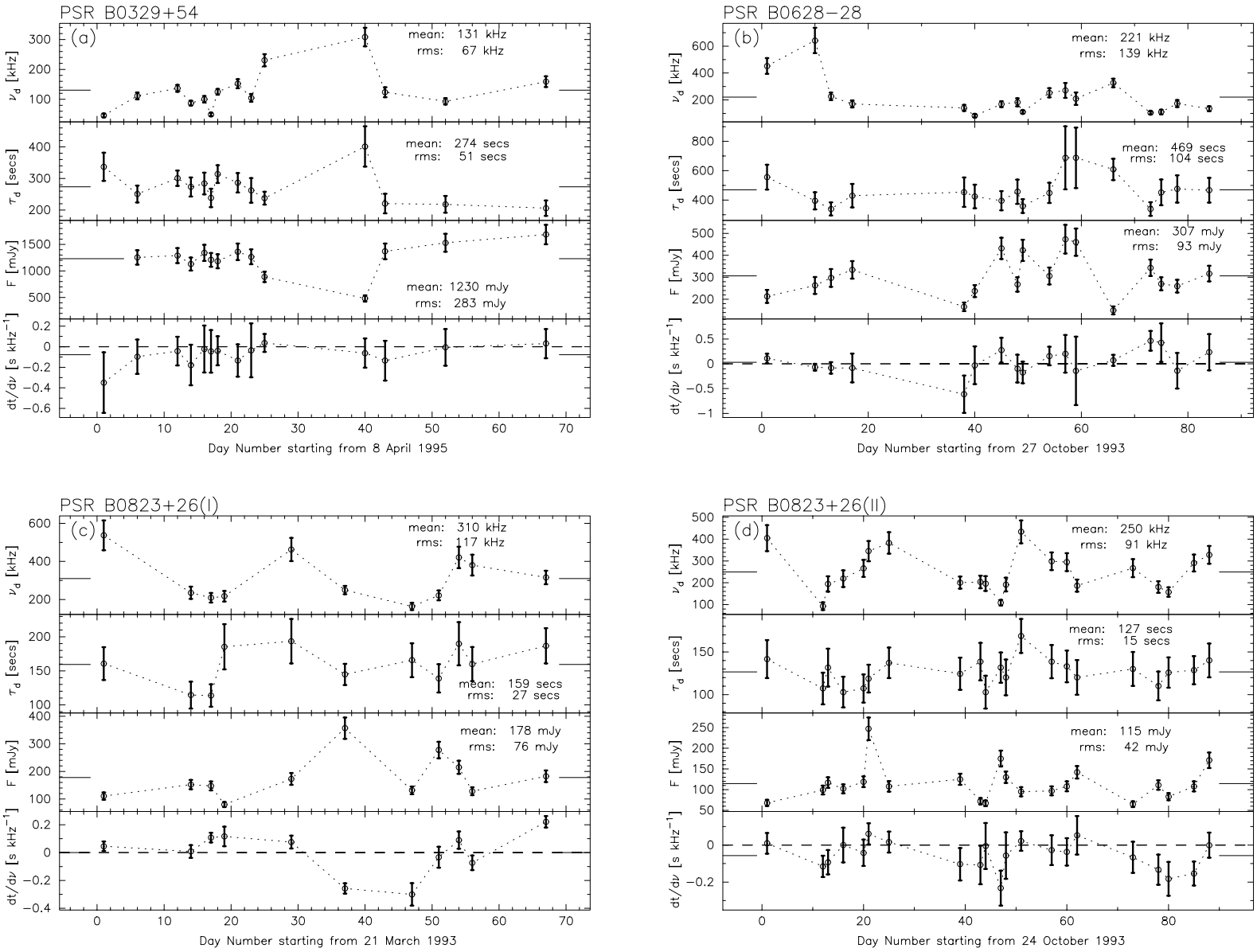

FIG. 4.—Time series of basic scintillation measurements: decorrelation bandwidth (v_d), scintillation timescale (τ_d), flux density (F), and drift rate of patterns (dt/dv). The uncertainties in the measurements indicate $\pm 1\ \sigma$ error estimates. The name of the pulsar and session ID (wherever needed) are given in the topmost panel of each figure. The solid markers (at either ends of the panel) indicate the average estimates of each time series. The dashed line in the plot of dt/dv corresponds to the zero drift slope. The starting date corresponding to the day 1 is given at the bottom of each figure (X-axis label). (*a*) PSR B0329 + 54; (*b*) PSR B0628 − 28; (*c*, *d*) data from the two observing sessions (I and II) of PSR B0823 + 26; (*e*)–(*h*) data from the four observing sessions (I to IV) of PSR B0834 + 06; (*i*) PSR B0919 + 06; (*j*, *k*) data of PSR B1133 + 16 for the observing sessions II and III; (*l*) PSR B1237 + 25; (*m*) PSR B1508 + 55; (*n*) PSR B1540 − 06; (*o*) PSR B1604 − 00; (*p*) PSR B1747 − 46; (*q*, *r*) data from the two observing sessions (I and II) of PSR B1919 + 21; (*s*) PSR B1929 + 10; (*t*) PSR B2016 + 28; (*u*) PSR B2020 + 28; (*v*) PSR B2045 − 16; (*w*) PSR B2310 + 42; and (*x*) PSR B2327 − 20.

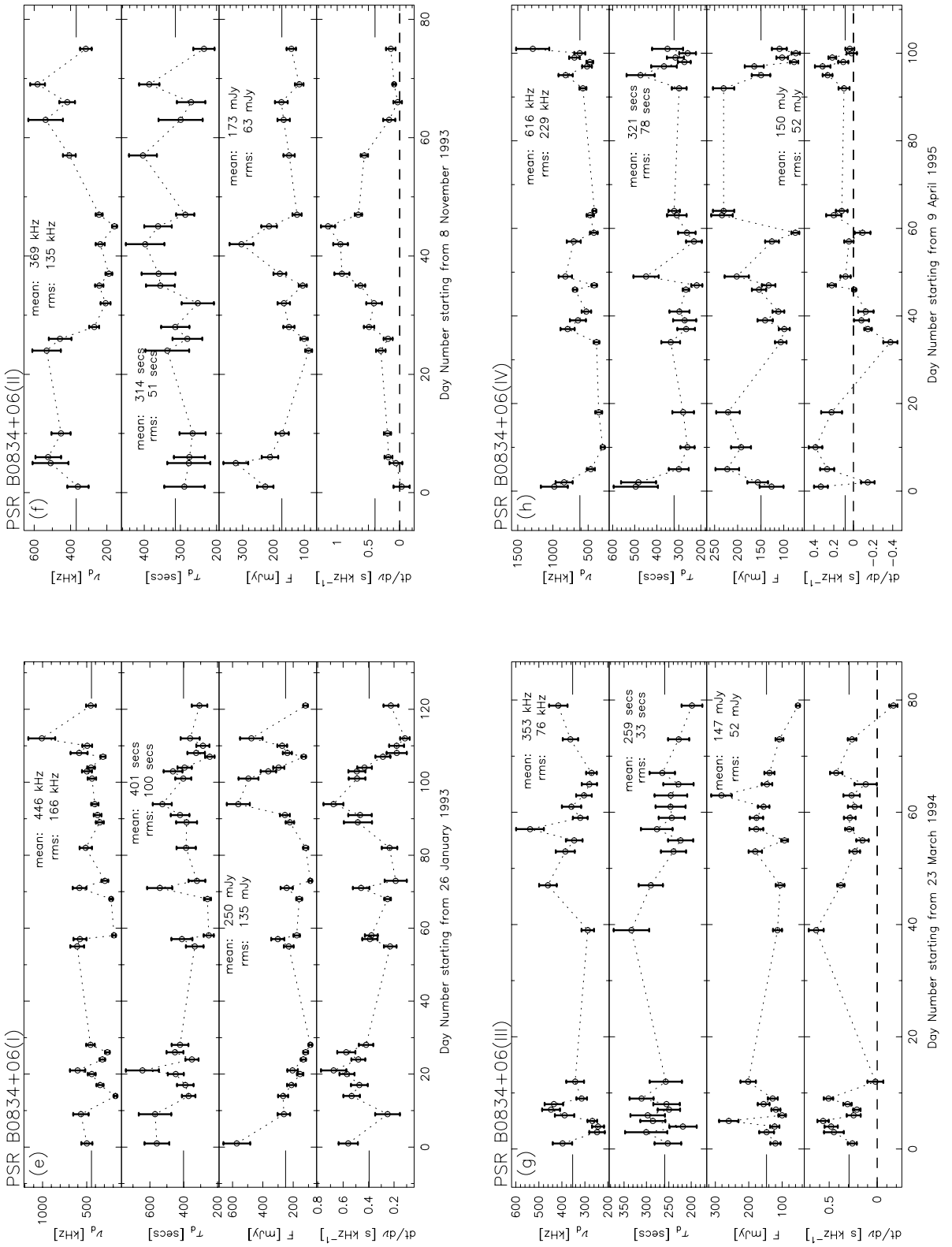

FIG. 4.—*Continued*

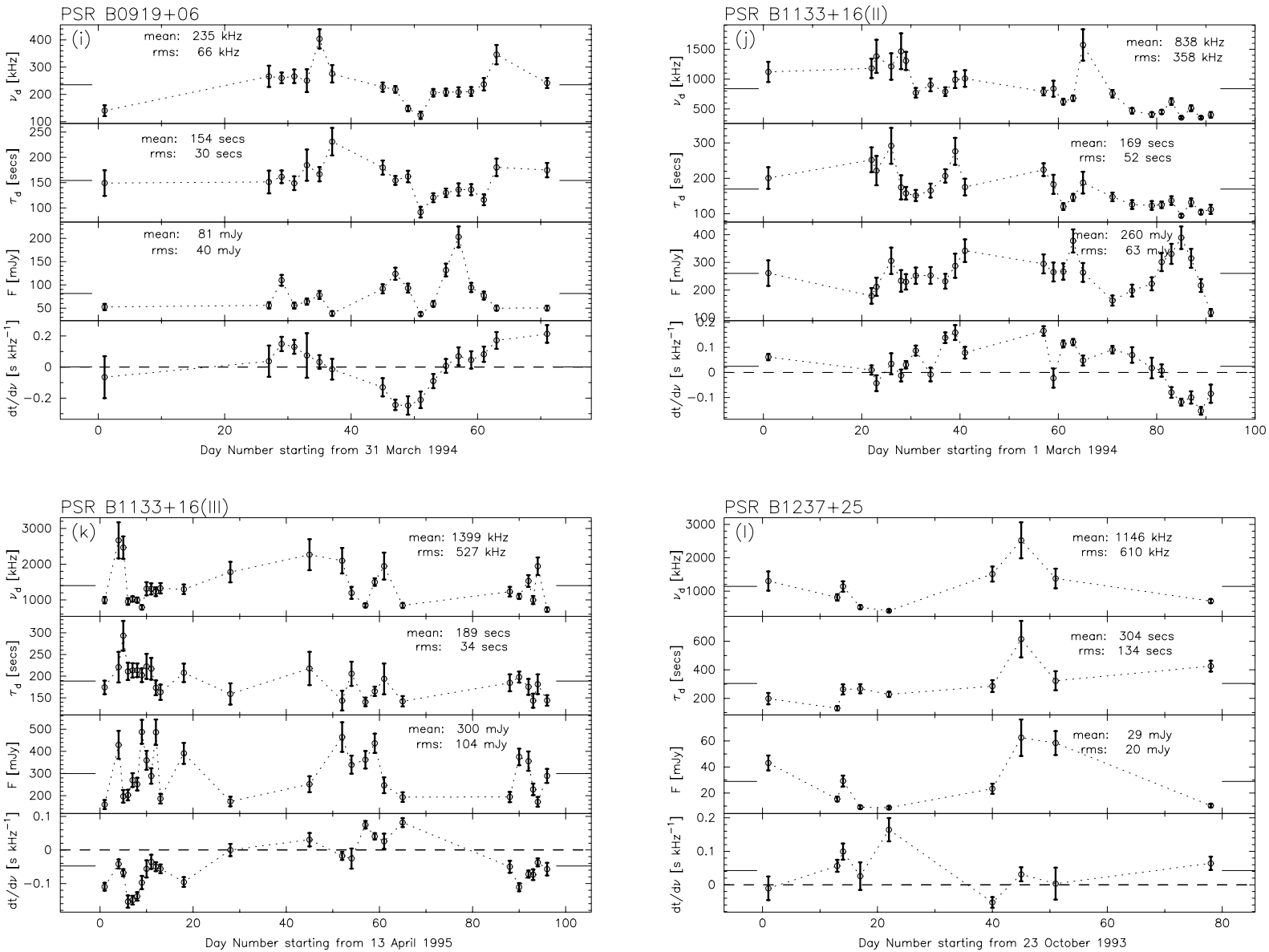

FIG. 4.—*Continued*

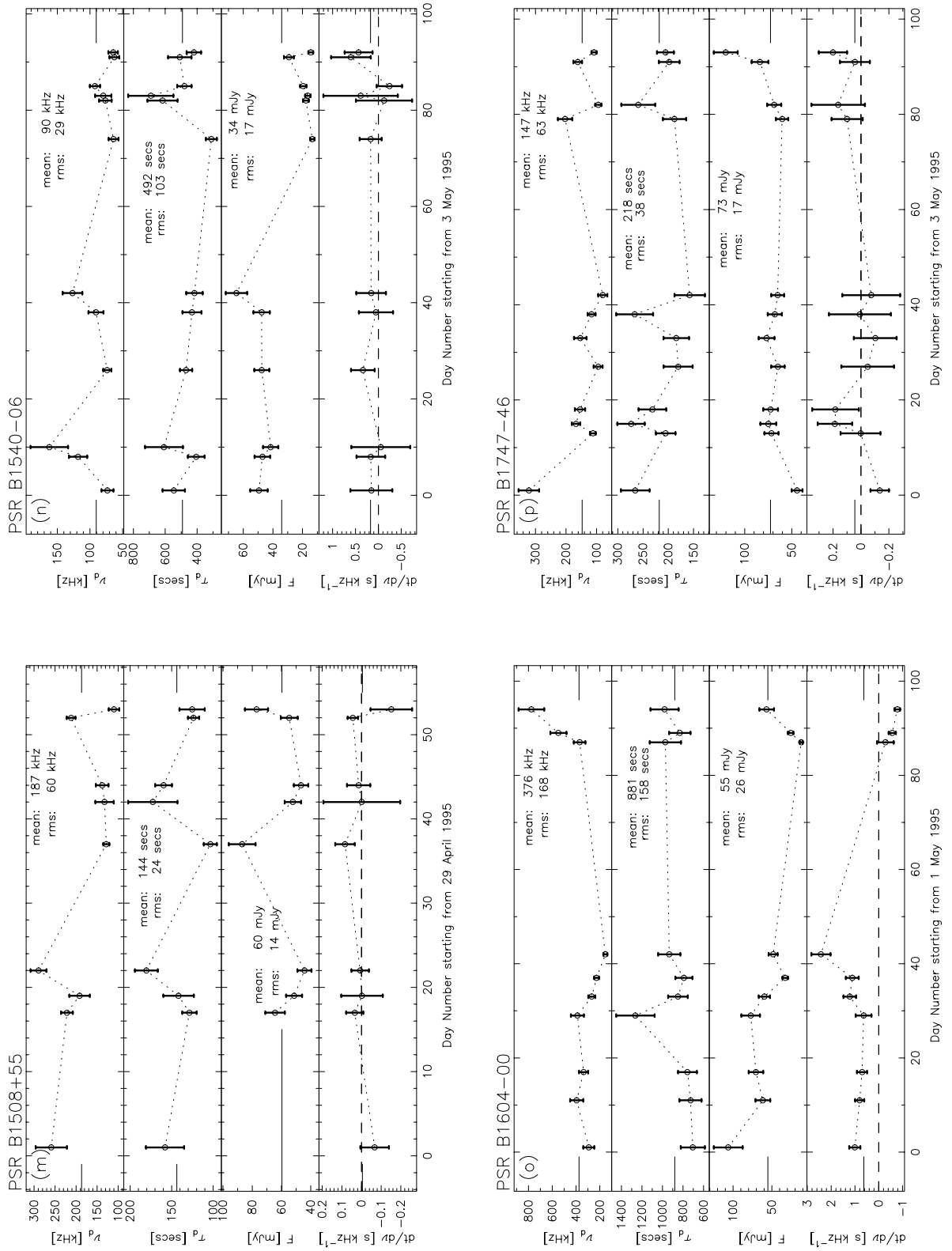

FIG. 4.—*Continued*

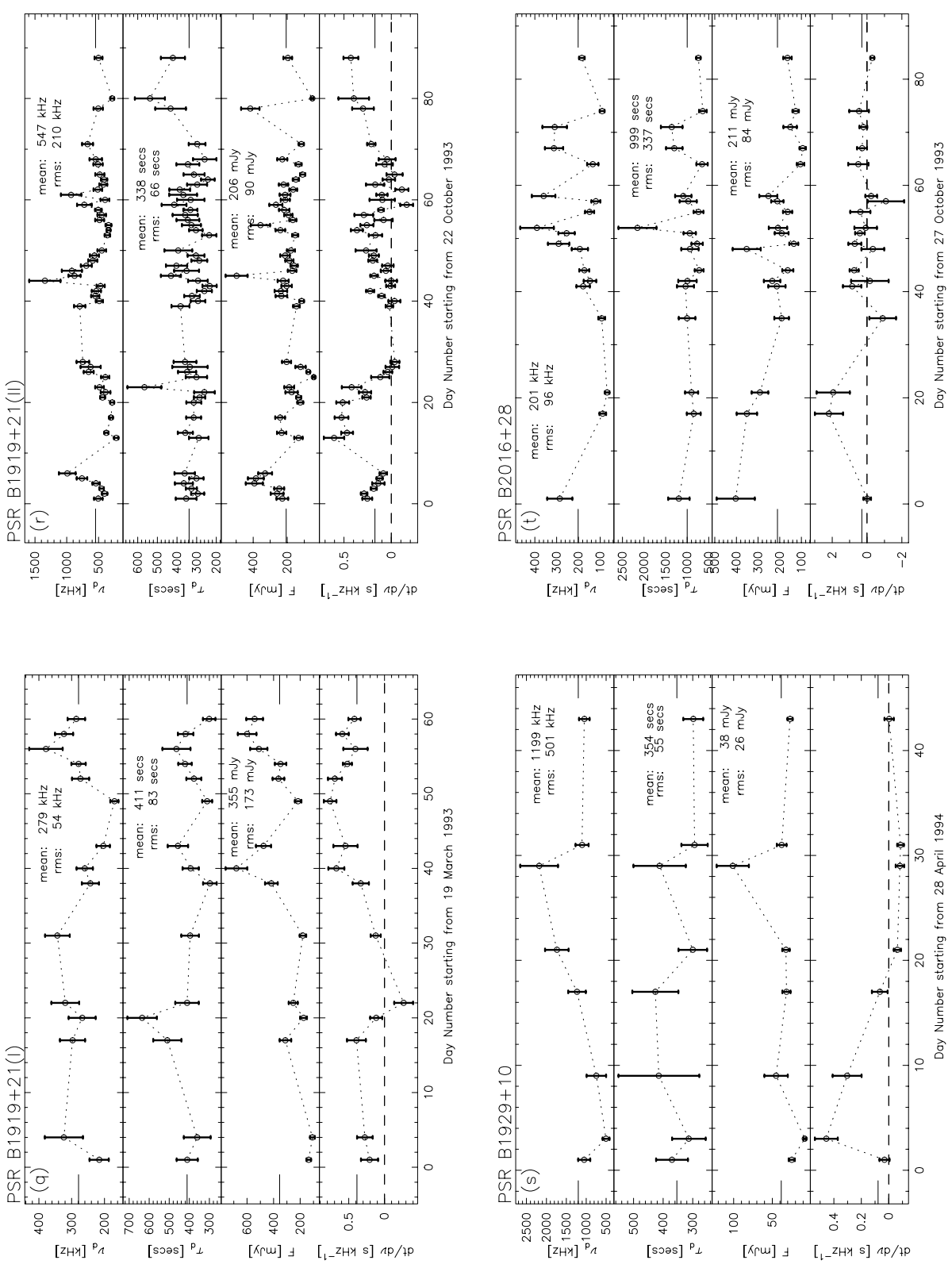

FIG. 4.—*Continued*

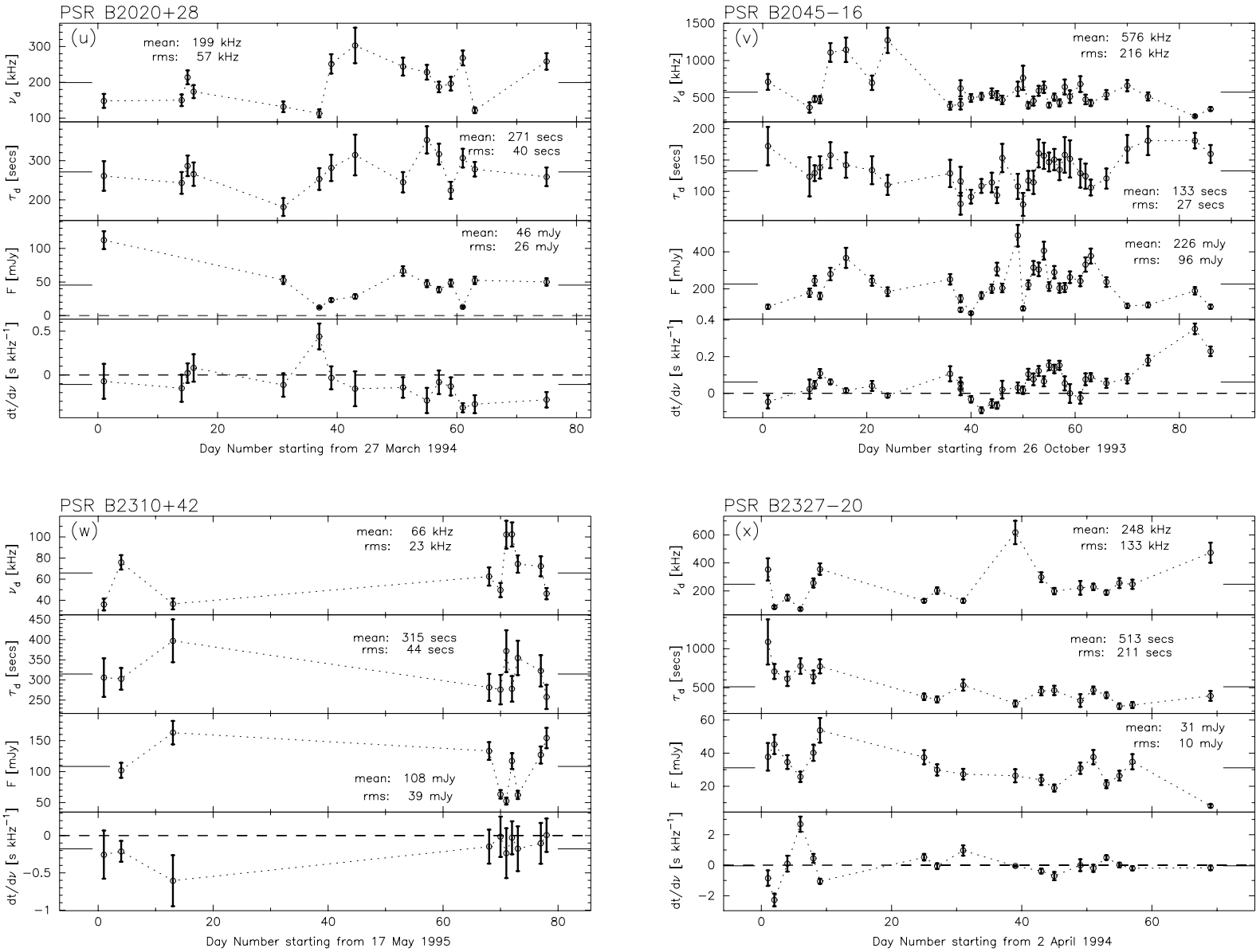

FIG. 4.—*Continued*

TABLE 3

MEASUREMENTS OF AVERAGE SCINTILLATION PARAMETERS

	TIME SERIES			GLOBAL ACF			OBSERVATIONAL PARAMETERS		
PULSAR (SESSION) (1)	$\langle v_d \rangle$ (kHz) (2)	$\langle \tau_d \rangle$ (s) (3)	$\langle dt/dv \rangle$ (s kHz^{-1}) (4)	$v_{d,g}$ (kHz) (5)	$\tau_{d,g}$ (s) (6)	$(dt/dv)_g$ (s kHz^{-1}) (7)	Δf_{ch} (kHz) (8)	Δt (s) (9)	N'_{ep} (10)
PSR B0329+54	130 ± 4	274 ± 9	−0.09 ± 0.04	165 ± 8	307 ± 19	−0.08 ± 0.25	140	07.15	15
PSR B0628−28	221 ± 8	469 ± 22	+0.04 ± 0.08	203 ± 11	456 ± 26	+0.09 ± 0.29	140	12.44	16
PSR B0823+26(IA).....	244 ± 15	150 ± 12	+0.11 ± 0.03	304 ± 12	145 ± 6	+0.11 ± 0.04	280	13.27	04
PSR B0823+26(IB).....	287 ± 18	160 ± 11	−0.12 ± 0.03	314 ± 14	162 ± 7	− 0.07 ± 0.06	140	13.27	06
PSR B0823+26(II).....	250 ± 8	127 ± 4	− 0.06 ± 0.02	261 ± 10	126 ± 5	− 0.05 ± 0.05	140	13.27	19
PSR B0834+06(IA).....	419 ± 14	413 ± 14	+ 0.41 ± 0.02	454 ± 11	391 ± 11	+ 0.39 ± 0.04	280	12.74	17
PSR B0834+06(IB).....	493 ± 22	381 ± 16	+ 0.38 ± 0.02	481 ± 13	353 ± 10	+ 0.33 ± 0.05	140	12.74	10
PSR B0834+06(II).....	369 ± 11	314 ± 11	+ 0.39 ± 0.02	375 ± 7	328 ± 7	+ 0.37 ± 0.04	140	12.74	18
PSR B0834+06(III).....	353 ± 8	259 ± 7	+ 0.29 ± 0.01	369 ± 4	255 ± 3	+ 0.28 ± 0.02	140	12.74	21
PSR B0834+06(IV).....	616 ± 17	321 ± 10	+ 0.08 ± 0.01	599 ± 7	309 ± 4	+ 0.08 ± 0.02	140	12.74	27
PSR B0919+06	235 ± 6	154 ± 4	+ 0.01 ± 0.02	256 ± 6	160 ± 4	− 0.01 ± 0.04	140	21.53	18
PSR B1133+16(I).....	434 ± 18	89 ± 4	+ 0.01 ± 0.01	543 ± 24	92 ± 4	+ 0.02 ± 0.03	280	11.88	06
PSR B1133+16(II).....	838 ± 21	169 ± 4	+ 0.03 ± 0.01	816 ± 11	165 ± 2	+ 0.05 ± 0.01	140	11.88	24
PSR B1133+16(III).....	1399 ± 33	189 ± 4	− 0.05 ± 0.01	1301 ± 12	192 ± 2	− 0.05 ± 0.01	140	11.88	28
PSR B1237+25	1146 ± 60	304 ± 16	+ 0.04 ± 0.01	1828 ± 174	439 ± 40	− 0.00 ± 0.06	140	13.82	09
PSR B1508+55(A).....	208 ± 9	139 ± 6	+ 0.03 ± 0.03	226 ± 6	164 ± 5	+ 0.03 ± 0.05	140	29.59	04
PSR B1508+55(B).....	148 ± 8	145 ± 9	− 0.02 ± 0.06	168 ± 15	158 ± 16	− 0.04 ± 0.21	140	14.79	04
PSR B1540−06	90 ± 3	492 ± 20	+ 0.22 ± 0.12	111 ± 5	526 ± 25	+ 0.22 ± 0.36	140	14.18	12
PSR B1604−00	376 ± 15	881 ± 38	+ 0.63 ± 0.08	379 ± 11	933 ± 30	+ 0.34 ± 0.19	140	21.09	10
PSR B1747−46(A).....	160 ± 7	230 ± 11	+ 0.01 ± 0.06	171 ± 7	239 ± 10	+ 0.02 ± 0.14	140	29.69	07
PSR B1747−46(B).....	130 ± 7	202 ± 11	+ 0.09 ± 0.07	158 ± 8	215 ± 11	+ 0.10 ± 0.14	140	14.85	05
PSR B1919+21(IA).....	295 ± 17	454 ± 25	+ 0.14 ± 0.05	338 ± 11	437 ± 14	+ 0.19 ± 0.08	280	13.37	06
PSR B1919+21(IB).....	269 ± 9	382 ± 14	+ 0.55 ± 0.04	285 ± 6	374 ± 9	+ 0.56 ± 0.06	140	13.37	09
PSR B1919+21(II).....	547 ± 11	338 ± 8	+ 0.17 ± 0.01	581 ± 9	339 ± 5	+ 0.13 ± 0.02	140	13.37	40
PSR B1929+10	1199 ± 83	354 ± 24	+ 0.08 ± 0.01	1293 ± 74	348 ± 19	− 0.01 ± 0.04	140	11.33	09
PSR B2016+28	201 ± 8	999 ± 41	+ 0.30 ± 0.14	206 ± 19	995 ± 100	+ 0.52 ± 1.07	140	13.95	19
PSR B2020+28	199 ± 5	271 ± 8	− 0.10 ± 0.03	270 ± 12	279 ± 12	− 0.17 ± 0.13	140	17.20	15
PSR B2045−16	576 ± 13	133 ± 3	+ 0.06 ± 0.01	539 ± 17	138 ± 4	+ 0.05 ± 0.02	140	19.62	29
PSR B2310+42	66 ± 3	315 ± 13	− 0.18 ± 0.09	114 ± 3	309 ± 9	− 0.12 ± 0.14	140	17.47	10
PSR B2327−20	248 ± 8	514 ± 18	− 0.04 ± 0.07	268 ± 18	432 ± 31	+ 0.06 ± 0.32	140	32.90	18

pairs averaged to get ρ_k (note that it is different from the quantity, ω_d, as defined in eq. [1]). Estimating the average scintillation parameters from the GACF has the following advantages over the time series averages: First, the individual ACFs are given weights proportional to their statistical reliabilities, which would make the average values less sensitive to ACFs computed from very short data stretches. The GACF has higher signal-to-noise ratios than the individual ACFs and is less sensitive to outliers, which results in smaller uncertainties in the fitting procedure. Further, while computing the GACF, deviations of the individual ACFs from their model Gaussians get averaged out, and so the GACF will be much closer to its model Gaussian form than the case of individual ACFs. The uncertainties due to the model fitting (σ_{mod}), which are largely attributable to the deviation from the Gaussian shape, will be smaller than that in the case of normal ACFs. Thus the estimates of average values obtained from this technique will be more robust than those from the time series. The only limitation is that the data should be taken with identical resolutions in time and frequency, which is the case with most of our data.

The GACFs obtained from our data are shown in Figure 5. For pulsars with multiple sessions of observations, GACF is computed for each session separately. In some cases, part of the data in a given session was obtained with a different resolution either in time or in frequency, in which case GACFs are computed for the corresponding data sets separately. In such cases, the labels A and B are attached along with the session ID [e.g., PSR B0823+26(IA)] or pulsar name [e.g., PSR B1508+55(A)] to distinguish between the different parts of data. The GACF is fitted with a Gaussian of the form described in equation (2) to yield parameters $v_{d,g}$, $\tau_{d,g}$, and $(dt/dv)_g$, which are the average estimates of v_d, τ_d, and dt/dv, respectively. These are presented in columns (5), (6), and (7), respectively, of Table 3. The values are, in general, comparable to the corresponding time series averages. However, there are some exceptions. For PSR B1237+25, the two methods give significantly different values. The estimates of $v_{d,g}$ and $\tau_{d,g}$ are larger than the time series averages. But, interestingly, the drift slope obtained from the GACF is very close to zero, in comparison to a significant value indicated by the time series. A similar property is also seen for PSR B1929+10. For PSR B1133+16(I), both methods yield significant average drift slopes, which may be because of its poor statistics ($N_{ep} = 6$). The discrepancy between the v_d values of PSR B2310+42 could be due its being close to the frequency resolution of our setup. This can be clearly seen from the time series, where v_d values corrected for instrumental smearing become lower than the resolution in frequency. For PSR

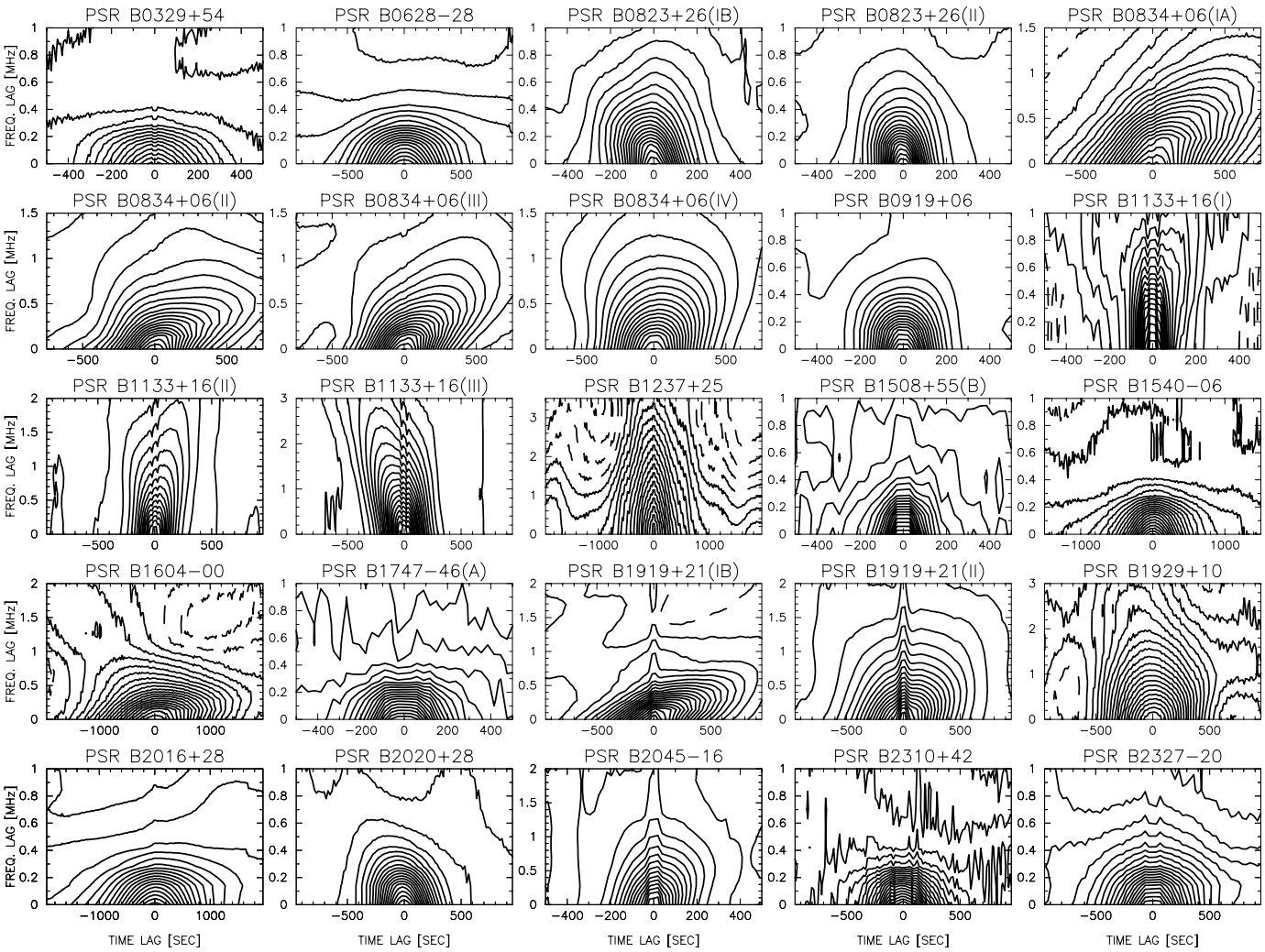

FIG. 5.—GACFs of 18 pulsars (25 data sets). The name of the pulsar is given at the top of each panel. For PSRs B0823+26, B0834+06, B1133+16, and B1919+21, there are multiple plots, which are GACFs computed for different observing sessions. The labels A and B represent the part of the data for which GACF is computed (see Table 3). GACFs represent the average scintillation properties. The plots shown here illustrate the general characteristics observed with the dynamic spectra of various pulsars and also variations in scintillation properties from pulsar to pulsar.

B2327−20, the discrepancy seen between $\langle \tau_d \rangle$ and $\tau_{d,g}$ seem to be due to some "outlier" data points in the initial epochs of observation. We believe the results from the GACF technique to be more robust than those from the time series and hence use them in our further analysis in this paper.

3.3.4. *Estimates of Derived Scattering Parameters and Pulsar Flux Densities*

Using the results obtained from the GACF method, we estimate some quantities characterizing the strength of scattering and scintillation pattern speed. The conventional way of describing the strength of scattering is in terms of C_n^2 (e.g., Rickett 1977; Cordes et al. 1985), where the spectrum of the plasma density fluctuations is considered to be a power law, given by $P_{\delta n_e}(\kappa) = C_n^2 \kappa^{-\alpha}$, where κ is the spatial wavenumber. The quantity C_n^2 is a measure of rms electron density fluctuations, which give rise to scattering. The line-of-sight average of C_n^2 is given by (Cordes et al. 1985),

$$\overline{C_n^2} = 2 \times 10^{-6} \, (f_{\rm obs,MHz})^{11/3} \, (D_{\rm pc})^{-11/6} \, (v_{d,\rm kHz})^{-5/6} \ {\rm m}^{-20/3} \ , \quad (7)$$

for a Kolmogorov form of density spectrum ($\alpha = 11/3$). Our estimates of C_n^2 are given in column (3) of Table 4, where the uncertainties are due to the measurement errors in $v_{d,g}$. In all our calculations, we make use of the most recent pulsar distance estimates available from Taylor, Manchester, & Lyne (1993, hereafter TML93), except for PSR B0823+26, for which an independent distance ($\approx$380 pc) from the parallax method is available (Gwinn et al. 1986). The new, improved estimates of $\overline{C_n^2}$ derived from our measurements have been used to study the distribution of scattering material in the local ISM (Bhat et al. 1997, 1998).

Another quantitative measure of the strength of scattering is the parameter u, which is defined as the ratio of the Fresnel scale ($s_{\rm F}$) to the "coherence scale" [$s_0 = (k\theta_s)^{-1}$]. In terms of decorrelation bandwidth, this quantity can be expressed as

$$u = \left(\frac{2 f_{\rm obs}}{v_d} \right)^{0.5} \quad (8)$$

(Rickett 1990; Gupta et al. 1994).

The values of u obtained from $v_{d,g}$ are given in column (4)

TABLE 4

DERIVED SCATTERING PARAMETERS AND PULSAR FLUX DENSITIES

							S_{400}	
NUMBER (1)	PULSAR (2)	$\log \overline{C_n^2}$ (3)	u (4)	V_{iss} (km s^{-1}) (5)	V_{prop} (km s^{-1}) (6)	S_{327} (mJy) (7)	G94[a] (mJy) (8)	TML93[b] (mJy) (9)
1.....	PSR B0329+54	-4.11 ± 0.019	63.0 ± 1.7	186 ± 17	145 ± 10	1230 ± 38	1565	1650
2.....	PSR B0628−28	-4.51 ± 0.020	56.8 ± 1.6	170 ± 15	180 ± 321	307 ± 9	422	200
3.....	PSR B0823+26(I)	-3.28 ± 0.012	46.0 ± 0.8	264 ± 14	196 ± 7	178 ± 6	78	65
4.....	PSR B0823+26(II)	-3.22 ± 0.015	50.1 ± 1.0	294 ± 18	...	115 ± 3	...	...
5.....	PSR B0834+06(I)	-3.94 ± 0.010	37.4 ± 0.5	184 ± 8	174 ± 20	250 ± 7	146	85
6.....	PSR B0834+06(II)	-3.86 ± 0.010	41.8 ± 0.6	187 ± 8	...	173 ± 5	...	...
7.....	PSR B0834+06(III)	-3.85 ± 0.007	42.3 ± 0.4	237 ± 7	...	147 ± 4	...	...
8.....	PSR B0834+06(IV)	-4.03 ± 0.008	33.0 ± 0.4	250 ± 8	...	150 ± 4	...	...
9.....	PSR B0919+06	-4.85 ± 0.010	50.5 ± 0.7	642 ± 26	919 ± 662	81 ± 2	55	60
10	PSR B1133+16(I)	-3.22 ± 0.018	34.7 ± 0.9	490 ± 38	475 ± 8	315 ± 14	95	300
11	PSR B1133+16(II)	-3.36 ± 0.008	28.3 ± 0.3	335 ± 10	...	260 ± 7	...	...
12	PSR B1133+16(III)	-3.53 ± 0.007	22.4 ± 0.2	363 ± 10	...	300 ± 7	...	...
13	PSR B1237+25	-4.24 ± 0.043	18.9 ± 1.1	271 ± 47	303 ± 13	29 ± 1	135	110
14	PSR B1508+55	-4.41 ± 0.018	57.6 ± 1.4	451 ± 35	913 ± 46	60 ± 2	105	95
15	PSR B1540−06	-3.80 ± 0.017	76.8 ± 1.8	80 ± 6	355 ± 222	34 ± 1	19	30
16	PSR B1604−00	-3.71 ± 0.018	41.5 ± 1.0	60 ± 5	20 ± 47	55 ± 2	98	60
17	PSR B1747−46	-3.89 ± 0.012	63.1 ± 1.1	218 ± 11	...	73 ± 2	...	70
18	PSR B1919+21(I)	-3.73 ± 0.011	45.9 ± 0.7	132 ± 6	122 ± 228	355 ± 12	72	200
19	PSR B1919+21(II)	-3.95 ± 0.007	33.6 ± 0.3	215 ± 7	...	206 ± 4	...	...
20	PSR B1929+10	-3.16 ± 0.029	22.5 ± 0.9	159 ± 19	86 ± 6	38 ± 3	450	250
21	PSR B2016+28	-3.98 ± 0.035	56.3 ± 2.7	56 ± 9	12 ± 19	211 ± 8	...	320
22	PSR B2020+28	-4.21 ± 0.017	49.2 ± 1.1	250 ± 18	97 ± 22	46 ± 1	...	110
23	PSR B2045−16	-3.90 ± 0.012	34.8 ± 0.6	501 ± 25	289 ± 71	226 ± 4	87	125
24	PSR B2310+42	-3.66 ± 0.011	75.7 ± 1.2	126 ± 6	...	108 ± 4	49	95
25	PSR B2327−20	-3.43 ± 0.025	49.4 ± 1.7	99 ± 11	...	31 ± 1	36	50

[a] Measurements at 400 MHz from Gould 1994.
[b] Measurements at 400 MHz from Taylor, Manchester, & Lyne 1993.

of Table 4, and they range from 20 to 75. The observable effects of refractive scintillation are thought to critically dependent on this parameter, and the condition $u > 1$ is considered to be the strong scattering regime. The quantity $\overline{C_n^2}$ is representative of average scattering along the line-of-sight, while u is an indicator of the integrated scattering at a given frequency of observation.

The scintillation pattern speed, V_{iss}, which measures the relative motion between the scintillation pattern and the observer, is estimated from measurements of decorrelation bandwidth and scintillation timescale (e.g., Cordes 1986) and is given by

$$V_{iss} = A_V \left[\frac{\sqrt{D_{kpc}\, \nu_{d,MHz}}}{(f_{obs,GHz}\, \tau_{d,s})} \right] \text{km s}^{-1} . \quad (9)$$

For the constant A_V, we adopt the value 3.85×10^4 given by Gupta et al. (1994). In the above expression, we have considered a thin screen placed midway between the pulsar and the observer. Values of V_{iss} derived from measurements of $\nu_{d,g}$ and $\tau_{d,g}$ are given in column (5) of Table 4 with uncertainties that reflect the measurement errors in $\nu_{d,g}$ and $\tau_{d,g}$. For pulsars PSRs B1747−46, B2310+42, and B2327−20, scintillation speeds are reported for the first time. Although V_{iss} represents the net effect of pulsar's proper motion (V_{prop}), Earth's orbital motion around the Sun (V_{obs}), and the bulk flow of the density irregularities in the ISM (V_{irr}), contributions due to V_{obs} and V_{irr} are usually small in comparison to those due to V_{prop}. Therefore, scintillation speeds are generally considered to be useful indicators of pulsar's proper-motion speeds.

The long-term nature of our observations have enabled us to obtain reliable flux density values by averaging out the fluctuations due to refractive scintillation. The average flux densities (S_{327}) are given in the column (7) of Table 4 and have measurement errors of the order of 5%. The uncertainties are due to absolute flux calibration and estimation error attributable to the finite number of scintles. Since the ORT is sensitive to linearly polarized radiation with electric field in the local north-south plane, our flux densities may turn out to be underestimates, especially for pulsars that have significant linearly polarized radiation.

4. DISCUSSION

We have presented results from a long-term systematic study of the scintillation properties of a large number of pulsars. Before we compare these average scintillation measurements with earlier studies and discuss the long-term stability of the scintillation parameters, we estimate the various errors in our computations of average scintillation properties. Two main sources of errors are (1) errors due to the finite number of independent epochs of observations, which we denote as σ_{meas}, and (2) errors due to limited number of refractive cycles of fluctuations spanned by the measurements, denoted as σ_{stat}. A direct estimation of the

latter is not practical; hence, we get first-order estimates by assuming a stationary statistics for RISS. This assumption may not be true for some pulsars, in which case our values of $\sigma_{\rm stat}$ will be less reliable. In the Appendix, we describe the details of our scheme for estimating these errors. The results of our error calculations are summarized in Table 5, which gives the percentage errors for $v_{d,g}$, $\tau_{d,g}$, and $\langle F \rangle$. In general, the second kind of errors dominate over the first kind; typical values of $\sigma_{\rm meas} \sim 2\%$–$5\%$, whereas those of $\sigma_{\rm stat} \sim 5\%$–$15\%$. Overall, our data represent a significant improvement in terms of accuracy and reliability of scintillation measurements compared to those available in the literature, most of which were obtained from observations at a few epochs. We now compare the present measurements of diffractive scintillation parameters ($v_{d,g}$ and $\tau_{d,g}$) and flux density ($\langle F \rangle$) with earlier measurements. We also examine the agreement between our estimates of scintillation speeds and the proper-motion speeds of pulsars.

4.1. *Comparison with Earlier Measurements*

4.1.1. *Decorrelation Bandwidth and Scintillation Timescale*

Measurements of decorrelation bandwidth and scintillation timescale reported in five papers—Cordes (1986), Cordes et al. (1985), Smith & Wright (1985), Roberts & Ables (1982), and Gupta et al. (1994)—have been scaled to our observing frequency assuming scaling laws $v_d \propto f_{\rm obs}^{4.4}$ and $\tau_d \propto f_{\rm obs}^{1.2}$, which correspond to a power-law spectral index $\alpha = 11/3$. The v_d and τ_d estimates calculated in this fashion are given in Tables 6 and 7. Whereas the measurements of Gupta et al. (1994) are from similar observations, i.e., from several epochs over a long period, the remaining ones are from fewer epochs.

As seen from Tables 6 and 7, there is a general lack of agreement between various measurements. Since refractive scintillation is thought to be the cause of slow fluctuations of diffractive observables, we first examine how well the discrepancies can be accounted for in terms of RISS-induced fluctuations. For pulsars PSR B1929+10 and PSR B2045−16, the differences between the measurements are within the rms fluctuations seen in our time series for v_d and therefore can be explained in terms of RISS. However, the discrepancies are much larger for the remaining pulsars. If we allow a 2 σ deviation from our average values, the discrepancies of 10 pulsars can be explained by RISS. For pulsars PSR B0919+06, PSR B1508+55, and PSR B1540−06, the discrepancies are much larger, and an RISS explanation may not be adequate. A partial explanation for pulsars PSR 0329+54 and PSR B1540−06 might be our instrumental limitations, because of which the intensity patterns are barely resolved in frequency, thereby making the v_d values less accurate.

Evidence for another reason that can give rise to large discrepancies can be found in our data itself. Interestingly, our observations show that average v_d values do not remain stable for pulsars PSR B0834+06, PSR B1133+16, and PSR B1919+21 from session to session, despite averaging over a time span of about 100 days for each session, much larger than their RISS timescales. Variations between the successive sessions of observations are found to be considerable, in some cases as much as a factor of 2–3. Thus our data show evidence for significant long-term variations of

TABLE 5

ERROR ESTIMATES ON SCINTILLATION MEASUREMENTS AND PULSAR FLUX DENSITIES

		MEASUREMENT ERRORS $\sigma_{\rm meas}$ (%)			STATISTICAL UNCERTAINTIES $\sigma_{\rm stat}$ (%)		
NUMBER (1)	PULSAR (SESSION) (2)	v_d (3)	τ_d (4)	F (5)	v_d (6)	τ_d (7)	F (8)
1	PSR B0329+54	5.3	6.3	3.4	18.3	7.8	10.6
2	PSR B0628−28	5.6	5.9	3.2	20.7	10.3	13.5
3	PSR B0823+26(I)	3.5	3.5	3.7	8.9	4.2	10.1
4	PSR B0823+26(II)	4.1	4.2	2.7	7.1	2.4	7.3
5	PSR B0834+06(I)	2.7	2.8	3.0	8.0	6.0	12.0
6	PSR B0834+06(II)	2.7	2.8	3.2	10.7	4.7	10.7
7	PSR B0834+06(III)	1.8	1.9	2.7	5.4	3.3	9.2
8	PSR B0834+06(IV)	2.1	2.1	2.9	7.5	4.9	6.9
9	PSR B0919+06	2.7	2.7	2.9	6.7	4.9	12.6
10	PSR B1133+16(I)	5.0	5.3	4.5	7.1	5.1	5.4
11	PSR B1133+16(II)	2.1	2.0	2.5	5.6	4.0	3.1
12	PSR B1133+16(III)	1.9	1.9	2.6	4.4	1.9	3.7
13	PSR B1237+25	11.8	11.6	8.1	5.0	4.7	10.5
14	PSR B1508+55	4.9	5.4	4.1	10.3	5.1	8.2
15	PSR B1540−06	4.7	5.1	3.8	16.2	12.5	30.6
16	PSR B1604−00	4.9	5.1	5.5	19.6	7.6	20.9
17	PSR B1747−46	3.4	3.5	3.4	13.1	5.7	8.1
18	PSR B1919+21(I)	3.0	3.1	3.5	6.9	8.5	19.8
19	PSR B1919+21(II)	2.1	2.1	2.2	8.0	4.5	9.8
20	PSR B1929+10	7.9	7.7	9.1	8.4	3.5	14.4
21	PSR B2016+28	9.6	10.4	4.1	31.0	22.4	26.4
22	PSR B2020+28	4.6	4.7	3.6	6.8	4.5	18.4
23	PSR B2045−16	3.3	3.3	2.2	5.9	2.8	6.2
24	PSR B2310+42	3.2	3.2	4.0	10.3	7.2	18.5
25	PSR B2327−20	7.0	7.4	3.2	21.0	20.6	13.9

TABLE 6

DECORRELATION BANDWIDTH MEASUREMENTS FROM THE LITERATURE

Pulsar (1)	$\nu_{d,g}$ (kHz) (2)	C86[a] (kHz) (3)	CWB85 (kHz) (4)	SW85[b] (kHz) (5)	RA82[c] (kHz) (6)	GRL94[b] (kHz) (7)
PSR B0329+54.....	165	28	...	11	...	18
PSR B0628+28.....	203	139	...	189	238	45
PSR B0823+26.....	293[d]	242	91[e]	189	...	71
PSR B0834+06.....	454[d]	188	69[e]	604	315	476
PSR B0919+06.....	256	36	14[e]	189	...	...
PSR B1133+16.....	816[d]	441	275[e]	491	...	...
PSR B1237+25.....	1828	451	230[e]	1511	...	...
PSR B1508+55.....	197	17	...	302	...	...
PSR B1540−06.....	111	197	...	...	...	...
PSR B1604−00.....	378	375	343[f]	1511	...	...
PSR B1747−46.....	165	...	...	...	...	...
PSR B1919+21.....	285[d]	175	33[f]	340	656	...
PSR B1929+10.....	1293	1009	946[f]	831	1439	...
PSR B2016+28.....	206	46	37[e]	113	...	35
PSR B2020+28.....	270	99	70[f]	227	...	...
PSR B2045−16.....	539	366	...	604	...	...
PSR B2310+42.....	114	...	...	...	...	...
PSR B2327−20.....	268	...	...	...	...	...

NOTE.—Sources for measurements are as follows: $\nu_{d,g}$, measurements from present observations; C86, Cordes 1986; CWB85, Cordes et al. 1985; SW85, Smith & Wright 1985; RA82, Roberts & Ables 1982; GRL94, Gupta et al. 1994.

[a] Scaled from values given at 1 GHz.

[b] Scaled from measurements at 408 MHz.

[c] Scaled from measurements at 335 MHz.

[d] Average of measurements of $\nu_{d,g}$ from different observing sessions

[e] Scaled from measurements at 430 MHz.

[f] Scaled from measurements at 320 MHz.

TABLE 7

SCINTILLATION TIME MEASUREMENTS FROM THE LITERATURE

Pulsar (1)	$\tau_{d,g}$ (s) (2)	C86[a] (s) (3)	CWB85[b] (4)	SW85[c] (s) (5)	RA82[d] (s) (6)	GRL94[c] (s) (7)
PSR B0329+54.....	307	147	...	253	...	149
PSR B0628+28.....	455	268	...	353	306	209
PSR B0823+26.....	126[e]	173	...	153	...	78
PSR B0834+06.....	390[e]	131	...	284	262	272
PSR B0919+06.....	160	63	...	207	...	...
PSR B1133+16.....	165[e]	77	...	184	...	...
PSR B1237+25.....	439	134	...	575	...	...
PSR B1508+55.....	158	34	...	138	...	...
PSR B1540−06.....	526	314	...	...	...	...
PSR B1604−00.....	933	688	...	767	...	...
PSR B1747−46.....	215	...	...	...	...	...
PSR B1919+21.....	374[e]	150	...	245	272	...
PSR B1929+10.....	348	353	...	376	379	...
PSR B2016+28.....	995	465	...	583	...	354
PSR B2020+28.....	279	293	...	245	...	...
PSR B2045−16.....	138	67	...	123	...	...
PSR B2310+42.....	309	...	...	...	...	...
PSR B2327−20.....	432	...	...	...	...	...

NOTE.—Sources are as follows: $\tau_{d,g}$, measurements from present observations; C86, Cordes 1986; CWB85, Cordes et al. 1985; SW85, Smith & Wright 1985; RA82, Roberts & Ables 1982; GRL94, Gupta et al. 1994.

[a] Scaled from values given at 1 GHz.

[b] Scintillation time measurements are not available.

[c] Scaled from measurements at 408 MHz.

[d] Scaled from measurements at 335 MHz.

[e] Average of measurements of $\tau_{d,g}$ from different observing sessions

strengths of scattering on timescales of ~years, something that has not been reported before. It is not very clear what can cause such effects, but they are difficult to understand in terms of RISS models based on simple power-law forms of density spectrum and a stationary statistics. Whatever the cause, such effects could explain the discrepancies seen in Tables 6 and 7. For example, PSR B1133+16 shows a systematic variation of $\langle v_d \rangle$ from 434 to 1434 kHz over a period of approximately 900 days, where $\langle v_d \rangle$ from the first session is in agreement with values from literature. Similarly, for PSR B0834+06, $\langle v_d \rangle$ values range from 350 to 610 kHz, which is comparable to the differences between our data and the earlier measurements (except the value from Cordes et al. 1985). Therefore, it is possible that the differences might be simply due to the measurements from observations made over separations of years.

The frequency scaling of decorrelation bandwidth is highly sensitive to the nature of the density spectrum assumed. The values listed, which are calculated for $\alpha = 11/3$, will substantially differ if the spectrum is steeper. The exact value of α is still uncertain, and there are conflicting interpretations from different scintillation experiments. Recently, Armstrong et al. (1995) have shown that the overall density spectrum in the nearby ISM ($\lesssim 1$ kpc), extending over about 10 orders of magnitude of scale sizes, is closer to a Kolmogorov form, but it is not clear if this is valid for all lines of sight. It is possible that an incorrect frequency scaling has also contributed, at least partially, to the present discrepancies.

The situation with τ_d measurements is similar, although the disagreements are less pronounced. Like the case with v_d values, RISS based on simple models fail to account for some of the observed discrepancies. It is possible that effects that can account for the discrepancies of v_d might explain the τ_d measurements as well. In addition, an apparent change in the scintillation pattern speed, due to reasons such as Earth's orbital motion ($V_{\rm obs}$) and bulk motion of the medium ($V_{\rm irr}$), can also lead to changes in τ_d. For example, in the case of PSR B2016+28, the variation of scintillation time due to Earth's motion is substantial (Gupta et al. 1994) and therefore dependent on the epoch of observation. Other pulsars where this effect is likely to be important are PSRs B1540−06 and B1604−00.

By and large, we find the discrepancies between our measurements (of both v_d and τ_d) and others to be more or less unbiased, except with those from Cordes et al. (1985). But we also note that the measurements given in Cordes (1986) are from a more extensive data set and later than those reported in Cordes et al. (1985). RISS seems to be the likely explanation for some of the discrepancies, but there are several exceptions for which an RISS explanation is inadequate. Long-term variations seen with $\langle v_d \rangle$ (e.g., for PSR B1133+16) can also be interpreted as large-scale spatial variations in C_n^2 (say, over ~50–100 AU), and this could be at least partly responsible for some of the unexplained discrepancies. Another possible source of discrepancies is an incorrect scaling of the measurements with frequency.

4.1.2. *Flux Density*

We compare our flux density measurements (S_{327}) (col. [7] of Table 4) with the known values from the literature. Measurements at 400 MHz (S_{400}) taken from Gould (1994, hereafter G94; for 15 pulsars) and TML93 are listed in columns (8) and (9) of Table 4. Our values, though less prone to errors due to RISS-induced fluctuations, may underestimate the true flux densities in the case of pulsars with a substantial fraction of linearly polarized radiation. On the other hand, it is possible that measurements from G94 and TML93 are not averaged out for fluctuations due to RISS. Our observations show large-amplitude variations in the flux density, where the individual measurements differ as much as by a factor 3–5. The considerable discrepancies (as much a factor 2–3) seen between the values from G94 and TML93 are, therefore, explicable in terms of RISS. Because of this, a detailed comparison between S_{327} and S_{400} may not be meaningful.

A first order comparison shows that, for nine pulsars, the two values are comparable. For PSRs B1540−06, B1604−00, B1747−46, and B2310+42, S_{327} is comparable to S_{400} from TML93. For PSR B1133+16, $\langle S_{327} \rangle \approx S_{400}$ from TML93; for PSR B1919+21, S_{327} from session II agrees with S_{400} of TML93. Similarly, the average values from sessions III–IV of PSR B0834+06 are comparable to S_{400} of G94. For PSR B0628−28, $S_{327} \approx \langle S_{400} \rangle$ (i.e., the average of S_{400} from G94 and TML93); for PSR B2327−20, $S_{327} \approx S_{400}$ from G94. For PSRs B0823+26, B0919+06, and B2045−16, our values are larger than S_{400} by a factor of ~1.5–2.5, whereas for PSRs B0329+54, B1508+55, B2016+28, and B2020+28, they are somewhat lower (~0.4–0.8 S_{400}). Two special cases are PSRs B1237+25 and B1929+10, for which S_{327} is considerably lower: by ~4 times for the former and by ~6–12 times for the latter. Such a large discrepancy can be attributed to the fact that these pulsars show a large fraction of linearly polarized radiation (with fractional linear polarizations [at 400 MHz] of ≈ 0.6 and ≈ 0.8, respectively), which can make our values underestimate the true values by a factor as much as ~3–5.

4.1.3. *Scintillation Pattern Speeds and Proper-Motion Speeds of Pulsars*

Scintillation speeds are considered to be good indicators of pulsar velocities and several authors have studied the correlation between the two (Lyne & Smith 1982; Cordes 1986; Gupta 1995, hereafter G95). In estimating scintillation speeds, different authors use different values for the constant A_V in equation (9). It was taken to be 2×10^4 by Lyne & Smith (1982), 1.27×10^4 by Cordes (1986), whereas Gupta et al. (1994) suggest a value of 3.85×10^4, which has been adopted by us. Our estimates (col. [5] of Table 4) are for a thin screen placed midway between the pulsar and the observer. More refined estimates can be obtained using the method described in Cordes & Rickett (1998) for a distributed scattering medium. It may be mentioned that the thin-screen method overestimates the scintillation speed compared to a uniformly distributed medium with a simple Kolmogorov form of density spectrum.

Proper-motion measurements are available for 15 of our pulsars (TML93 and references therein). We have used them in combination with most recent distance estimates (Taylor et al. 1993) to estimate the pulsar velocities ($V_{\rm prop}$) and these are given in column (6) of Table 4. Values of $V_{\rm prop}$ are highly uncertain for four pulsars (PSRs B0628−28, B1604−00, B1919+21, and B2016+28), because the error in the measurement is larger than the estimate of the proper motion itself. Also, for PSRs B0919+06 and B1540−06, there are considerable uncertainties (60%–70%). For the rest of the pulsars, the uncertainties in $V_{\rm prop}$ are $\lesssim$ 25%. These uncer-

tainties are due solely to the measurement errors in proper motions. Taking into consideration the errors in distance estimates (typically 25%), the actual errors in $V_{\rm prop}$ will be much larger for most pulsars.

Taking into consideration the uncertainties in $V_{\rm iss}$ and $V_{\rm prop}$, one can see that, for a number of pulsars, $V_{\rm iss}$ is a reasonably good indicator of the proper-motion speed. A plot of $V_{\rm prop}$ versus $V_{\rm iss}$ is shown in Figure 6, where a significant correlation between the two can be seen (correlation coefficient of 0.75). The best agreement between $V_{\rm iss}$ and $V_{\rm prop}$ is seen for PSR B1237+25. The measurements are consistent for PSR B0919+06, but here the uncertainty in the proper motion is very large (70%). For PSRs B0834+06 and B1133+16, $V_{\rm iss}$ estimates from part of the data agree with $V_{\rm prop}$. If we consider 3 σ uncertainties in both $V_{\rm iss}$ and $V_{\rm prop}$, the two speeds are consistent for a fairly large number of measurements. Two exceptional cases are PSR B1508+55, with $V_{\rm iss} \approx 0.5 V_{\rm prop}$, and PSR B2020+28, with $V_{\rm iss} \approx 2.5 V_{\rm prop}$. For PSR B1508+55, the observed discrepancy is consistent with the estimated "z-height" of this pulsar and the expected "z-height" of the electron density layer in the Galaxy, as discussed in detail in G95. For PSR B2020+28, our observations confirm the discrepancy noted by G95. The likely explanation for this is enhanced scattering from the Orion arm of the Galaxy, as postulated in G95. Significant discrepancies are also seen for PSR B0823+26(II), PSR B1133+16(II), and PSR B1133+16(III).

By and large, scintillation speeds can be used as rough indicators of proper-motion speeds. The discrepancies seen can result from the distance estimate used and/or an asymmetric location of the effective scattering screen (see G95). Estimates of $V_{\rm iss}$ are comparatively less prone to distance uncertainties but critically depend on the relative location of the scattering screen with respect to the pulsar and the observer. A detailed treatment of such discrepancies is beyond the scope of the present work. The question of long-term stability of $V_{\rm iss}$ also seems to have some relevance, since we find some evidence for significant variation in $V_{\rm iss}$ between different observing sessions for PSRs B0834+06, B1133+16, and B1919+21, much in contradiction with the general expectations. We discuss the issue of long-term ($\sim$yr) stability of v_d, τ_d, and $V_{\rm iss}$ in the following section.

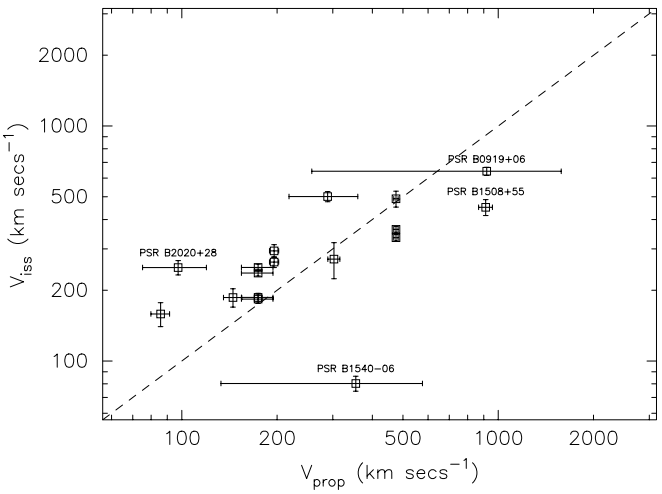

FIG. 6.—Available proper-motion speeds ($V_{\rm prop}$) of 11 pulsars are plotted against their scintillation speeds ($V_{\rm iss}$) derived from the present scintillation measurements. The dashed line is of unity slope.

4.2. *Long-Term Stability of Scintillation Properties and Pulsar Fluxes*

On the basis of results obtained from the observations of four pulsars for which we have multiple observing sessions (PSR B0823+26, PSR B0834+06, PSR B1133+16, and PSR B1919+21), we briefly discuss the issue of long-term stability (i.e., over timescales much larger than RISS timescales) of scintillation properties and pulsar fluxes. Observations were made over a fairly large number of epochs, spanning sufficiently long time spans (66–120 days), except PSR B1133+16(I), where the statistics is poor in terms of the number of measurements ($N_{\rm ep} = 6$), and the observations span only 19 days. The two sessions of PSRs B0823+26 and B1919+21 span 305 days, and the data of PSRs B0834+06 and B1133+16 cover $\approx$930 days. This data allow us to examine the stability of measurements over timescales much larger than RISS timescales for these pulsars.

In general, we find the basic scintillation properties v_d and τ_d vary significantly between successive observing sessions. Sometimes, considerable variations are seen in the average flux densities as well. The observed long-term variations in the average values $\langle v_d \rangle$, $\langle \tau_d \rangle$, $\langle F \rangle$, and $V_{\rm iss}$ (i.e., computed using $v_{d,g}$ and $\tau_{d,g}$, as described in § 3.3.4) are summarized in Figure 7. The uncertainties shown by the vertical error bar are estimated as $(\sigma^2_{\rm meas} + \sigma^2_{\rm stat})^{0.5}$. The horizontal bar represents the time span of observation.

The changes in $\langle v_d \rangle$ of PSR B0823+26 between the two sessions are within their statistical uncertainties, but the 18% reduction in $\langle \tau_d \rangle$ and the $\sim$13% increase in $V_{\rm iss}$ are larger than the uncertainties. The increase in $V_{\rm iss}$ can be explained by the transverse component of Earth's orbital motion ($V_{\rm obs\perp}$) to the line-of-sight to this pulsar, which increases from ≈ -1 km s^{-1} in the first session to $\approx$19 km s^{-1} in the second. This naturally explains the apparent reduction in $\langle \tau_d \rangle$. However, the 35% reduction in $\langle F \rangle$ from session I to II is not reconcilable within the uncertainties (at $\pm 1\,\sigma$ level).

For PSR B0834+06, measurements of $\langle v_d \rangle$ are stable (within the uncertainties) for the first three sessions, but there is $\sim$75% increase from III to IV; $\langle \tau_d \rangle$ also shows a similar trend between these two sessions, showing a 24% increase, whereas $V_{\rm iss}$ and $\langle F \rangle$ remain stable within the measurement errors. The variation of $\langle v_d \rangle$ and $\langle \tau_d \rangle$ between the sessions III and IV can be understood by a reduction of effective scattering strength ($\int C_n^2$) by $\sim$30%. The expected $\langle \tau_d \rangle$ of 340 s ($\tau_d \propto \theta_s^{-1}$) is consistent with the measured value 322 $\pm$ 17 s. The reason for such a variation of C_n^2 is, however, unclear.

Although $\langle v_d \rangle$ remains more or less stable from session I to III for PSR B0834+06, there is a steady and significant reduction in $\langle \tau_d \rangle$, which is also reflected as an increase in $V_{\rm iss}$. This pulsar is known to have a proper motion of 174 $\pm$ 20 km s^{-1}, which is consistent with $V_{\rm iss}$ measurements from the sessions I and II. The change in $\langle V_{\rm obs\perp} \rangle$ from $\approx$11 km s^{-1} to $\approx$19 km s^{-1} can only partly account for the decrease in $\langle \tau_d \rangle$ between the sessions I and II. Similarly, $\langle V_{\rm obs\perp} \rangle$ values of sessions I and IV, 11 and -15 km s^{-1}, imply a relative change of $\sim$26 km s^{-1} in $V_{\rm iss}$, which is about 50% of the observed variation. Thus the variations of $\langle \tau_d \rangle$ are only partially explainable in terms of $V_{\rm obs}$. Further,

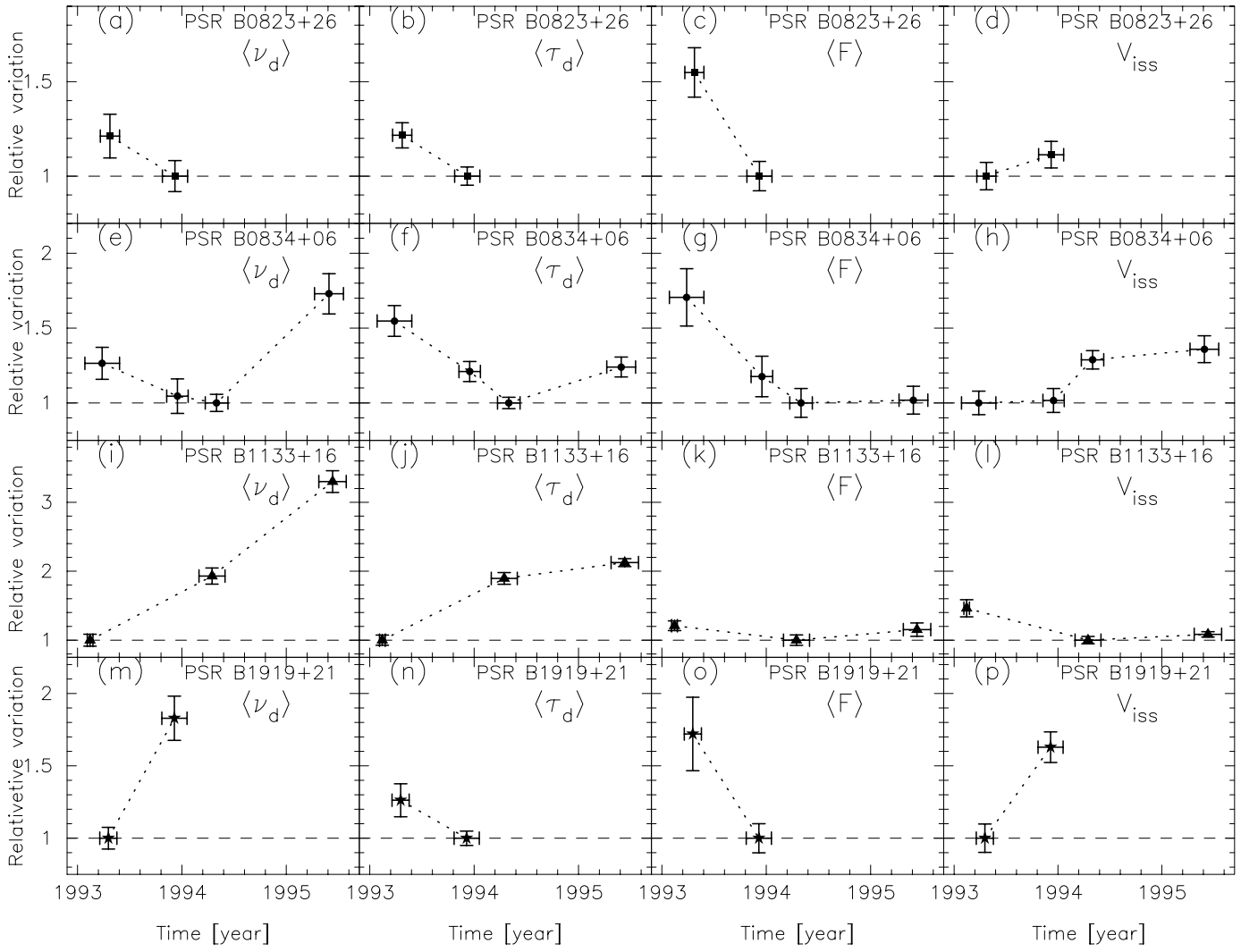

FIG. 7.—Plots illustrating the long-term (~several months to 1 yr) variations in the average scintillation properties ($\langle v_d \rangle$, $\langle \tau_d \rangle$, and V_{iss}) and pulsar flux densities ($\langle F \rangle$). The pulsar name and the quantity plotted are given at the top of each panel. The vertical bar is the total uncertainty due to measurement and statistical errors. The horizontal bar represents the length of observing time span. The measurements are normalized to unity for their lowest values.

there is a significant reduction (by 30%) in $\langle F \rangle$ from session I to II, which cannot be reconciled in terms of RISS modulations.

Long-term variations of scintillation characteristics of PSR B1133+16 are much more complex than the rest of the pulsars. There is a factor of 2 increase in $\langle v_d \rangle$ and $\langle \tau_d \rangle$ between the sessions I and II. The variations in $\langle v_d \rangle$ and $\langle \tau_d \rangle$ are not consistent with a simple reduction in the scattering strength (C_n^2); $\langle v_d \rangle$ shows a remarkable increase between the sessions II and III, whereas $\langle \tau_d \rangle$ and $\langle F \rangle$ remain more or less stable. These variations are reflected in the estimated V_{iss} values, which range from 335 ± 10 km s^{-1} (in session II) to 490 ± 38 km s^{-1} (in the initial session). This pulsar also exhibits remarkable long-term changes in the dynamic spectra, where v_d ranges from values as low as ~300 kHz (at some epochs of initial session) to as large as ~7 MHz (at some epochs of session III). This is a unique pulsar that shows three different "modes" of scintillation: (1) $v_d \sim$ a few 100 kHz and $\tau_d \sim 100$ s (session I and second half of session II), (2) $v_d \sim 1$ MHz and $\tau_d \sim 200$ s (first half of session II), and (3) $v_d \sim$ several MHz and $\tau_d \sim 200$ s (session III). The long-term variability of scintillation properties of this pulsar cannot be explained in terms of RISS, variations in the strength of scattering (C_n^2), or the effect due to the Earth's orbital motion. It may also be mentioned that this pulsar is fairly close by ($D \approx 270$ pc) and is known to have shown multiple imaging events (Hewish et al. 1985; Cordes & Wolszczan 1986; our observations).

For PSR B1919+21, substantial changes are seen in $\langle v_d \rangle$ and $\langle \tau_d \rangle$ but with opposite trends. This is also reflected as a remarkable (~70%) increase in V_{iss} from session I to II. This pulsar is known to have a proper motion $V_{prop} \sim 122 \pm 228$ km s^{-1}, which will be consistent with V_{iss} estimate from either of the sessions. The increase in $\langle v_d \rangle$ from 279 to 510 kHz between the two sessions implies a reduction in the small-scale scattering ($\int C_n^2$) by ~ 35%, which would have resulted in $\langle \tau_d \rangle \sim 555$ s if $V_{iss} \approx V_{prop}$ for both the sessions. The discrepancy in the two V_{iss} values are not reconcilable within the uncertainties due to refractive modulations. On examining the effect of the Earth's orbital motion on V_{iss} measurements of this pulsar, we find the relative change in $\langle V_{obs\perp} \rangle$ to be ≈ 30 km s^{-1} ($\langle V_{obs\perp} \rangle$ values are ≈ -5 km s^{-1}

and ≈ 25 km s^{-1} for the sessions I and II, respectively). The effect of observer's motion can, therefore, only partly account for the discrepancy. The bulk flow of the density irregularities ($V_{\rm irr}$) is another possible explanation of discrepancy, but the required $V_{\rm irr} \sim 55$ km s^{-1} is highly improbable. Bondi et al. (1994), based on their 1 yr flux modulation studies of low-frequency variables, argue that $V_{\rm irr} < 10$ km s^{-1}. Thus the observer's motion and the motion of the medium do not satisfactorily account for the observed variability of $V_{\rm iss}$ values. Another effect that can give rise to modulation of $V_{\rm iss}$ is the angular wandering of the source position caused by the refractive effects, which we will discuss in a subsequent paper. There is 42% reduction in $\langle F \rangle$ from session I to II, which is significantly larger than the statistical fluctuations that can be expected due to RISS.

Systematic observations to study the long-term stability of basic scintillation properties (v_d and τ_d) and pulsar fluxes have not been attempted before. The present observations show some evidence to suggest that these quantities do not remain stable for *some* pulsars despite averaging over periods much longer than the RISS timescale. Such a property is unexpected from the current RISS models. Normal RISS is expected to give rise to fluctuations of scintillation observables over refractive timescales, and no ISS effect is known to date that can cause the long-term (session-to-session) variations seen in the present observations. Since the measurements have been made with the same experimental setup, an observational bias is highly unlikely. The observed variations of $\langle v_d \rangle$ and $\langle \tau_d \rangle$ cannot be fully attributed to effective changes in scattering strength C_n^2 and/or the effect due to Earth's orbital motion around the Sun. Substantial variations of C_n^2 are not expected over the transverse extents of $\sim$50–100 AU that has been probed by the present data. The observed variability of the flux is also anomalous, and there are no intrinsic or extrinsic effects known that can produce significant flux variations over timescales $\sim$1–2 yr. All these conclusions are, however, based on only *three* pulsars; systematic observations of more pulsars are needed for a better understanding of these effects.

5. SUMMARY AND CONCLUSIONS

We have made an extensive series of scintillation observations for 18 pulsars in the DM range 3–35 pc cm^{-3} using the ORT at 327 MHz. The dynamic scintillation spectra of these pulsars were monitored at 10–90 epochs over time spans of 100–1000 days during 1993–1995. In this paper, we have presented the basic results from these observations. Some of the implications of these results, such as constraints on the spectrum of electron density fluctuations in the ISM and implications for the theoretical models of refractive scintillation, are addressed in two subsequent papers.

Two-dimensional autocovariance functions (2D ACF) were computed for the dynamic spectra and are used to estimate quantities such as decorrelation bandwidth (v_d), scintillation timescale (τ_d), and the drift rate of intensity patterns (dt/dv) for each observation. Time series of these quantities and flux density (F) are presented and can be used to investigate various refractive effects in pulsar scintillation. All four quantities show large-amplitude fluctuations (as much as by a factor 3–5) over time spans of about 100 days and are also found to vary significantly over timescales as short as a few days.

Several pulsars show pronounced drifting of intensity patterns in dynamic spectra, of which PSRs B0834+06, B1133+16, B1919+21, and B2045−16 form some of the best examples. For many pulsars, the measured drift slopes (dt/dv) show gradual variations with time and undergo several sign reversals during the observing time spans. Data of PSRs B0823+26, B0919+06, and B2020+28 illustrate this property, which is in accordance with the expectations of RISS theory. However, there are some pulsars for which no sign reversals of the drift slopes are seen over many months. Data of PSRs B0834+06 and B1919+21 are best examples of such "persistent drifts." Out of the four well-separated observing sessions of PSR B0834+06 spanning $\sim$1000 days, persistent drifts are observed in the first three, whereas the data from the final session show several occasions of sign reversals of pattern slopes.

PSR B1133+16, which was observed for three sessions spanning $\sim$1000 days, shows remarkable changes in its dynamic spectrum from one session to another. The data from the initial session are characterized by scintles that are fairly narrow in both time ($\sim$100 s) and frequency ($\sim$300 kHz). The data taken 1 yr later show much broader scintles ($\sim$200 s and $\sim$1 MHz). An episode of "interstellar fringing" is observed on 1994 April 30, which is followed by data characterized by narrower scintles (similar to the first session). Data from the final session show patterns that decorrelate over a wider range of frequency ($\sim$2 MHz) and time ($\sim$200 s). Such dramatic variations are not seen for any other pulsar. The pulsar PSR B1919+21 is found to show fine, deep intensity modulations over and above random intensity modulations in time and frequency caused by ISS. These modulations occur over typical timescales of a minute (much shorter than DISS timescale) with level of modulations as much as 50%. The modulations are broadband and persist throughout our observations, which suggests that they are intrinsic to the pulsar.

To obtain more reliable estimates of the average values of v_d, τ_d, and dt/dv from all the observations of a given pulsar, we have computed the Global ACF (GACF) for each pulsar. Whereas the results from GACF and time series methods agree in general, there are considerable differences in some cases, especially when the statistics is poor. Since the GACF method is expected to yield more robust estimates of the average properties, we prefer them over the time series averages. Estimates of decorrelation bandwidth ($v_{d,g}$) and scintillation timescale ($\tau_{d,g}$) from GACFs are used to estimate parameters such as the line-of-sight–averaged strength of scattering ($\overline{C_n^2}$), the strength of scattering parameter (u), and the scintillation pattern speed ($V_{\rm iss}$). A comparison between the scintillation speeds derived from our measurements and proper-motion speeds of pulsars show that scintillation speeds are reasonably good indicators of proper-motion speeds.

The present observations have resulted in a significant improvement in terms of accuracy and reliability of the scintillation measurements compared to those available in the published literature. For pulsars PSRs B1747–46, B2310+42, and B2327–20, scintillation parameters are reported for the first time. There are considerable differences between our measurements of decorrelation bandwidth and scintillation timescale and various earlier measurements. Although RISS seems to be a likely explanation for some of the differences, it does not satisfactorily account for all discrepancies.

There is some evidence from our data for fluctuations of scintillation properties and flux densities over timescales much longer than that of RISS. For pulsars studied over multiple sessions, significant variations from session to session are sometimes seen in one or more of the parameters $\langle v_d \rangle$, $\langle \tau_d \rangle$, and $\langle F \rangle$. Long-term ($\sim$1 yr) variations of this kind are not expected from current RISS models. Some of the variations of $\langle \tau_d \rangle$ can be accounted for by variations in scintillation pattern velocities due to the Earth's orbital motion. The $\langle v_d \rangle$ variations indicate variations of strengths of scattering along certain lines of sight. No obvious explanation can be found for the variations of $\langle F \rangle$. Possible implications of these results are a nonstationary nature of the ISM over $\sim$50–100 AU or some hitherto unidentified form of ISS.

The authors would like to thank J. Chengalur and M. Vivekanand for a critical reading of the manuscript and for giving useful comments. We thank V. Balasubramanian for the telescope time and technical help with the observations. We also thank the staff of Radio Astronomy Centre, Ooty, for their assistance with the observations. We thank our referee for comments that helped us clarify a number of things related to the work presented in this paper.

APPENDIX

SOURCES OF ERRORS ON THE AVERAGE SCINTILLATION PROPERTIES AND FLUX DENSITIES

Here we estimate the errors on the average values of scintillation properties [$v_{d,g}$, $\tau_{d,g}$, and $(dt/dv)_g$] and flux density ($\langle F \rangle$). These include (1) the measurement error ($\sigma_{\rm meas}$) and (2) the statistical error due to the number of refractive cycles spanned by the measurements ($\sigma_{\rm stat}$). The measurement error depends largely on the number of epochs of measurements ($N_{\rm ep}$). For $v_{d,g}$, $\tau_{d,g}$, and $(dt/dv)_g$, which are estimated from GACF, $\sigma_{\rm meas}$ has contributions mainly from two sources: the error from the Gaussian fit (as described in § 3.3.1) to the GACF (denoted as $\sigma_{{\rm mod},g}$) and the estimation error due to the finite number of scintles contributing to the GACF (denoted as $\sigma_{{\rm est},g}$). To compute $\sigma_{{\rm est},g}$, we treat $v_{d,g}$ and $\tau_{d,g}$ as representatives of a single dynamic spectrum of duration $\sum_{i=1}^{i=N_{\rm ep}} t_{{\rm obs},i}$, where $t_{{\rm obs},i}$ is the duration of observation at the ith epoch. The fractional estimation error ($\sigma_{{\rm est},g}$) is given by

$$\sigma_{{\rm est},g} = \left[f_d \left(\frac{\sum_{i=1}^{i=N_{\rm ep}} B_{{\rm obs},i}\, t_{{\rm obs},i}}{v_{d,g}\, \tau_{d,g}} \right) \right]^{-0.5}, \tag{A1}$$

where $B_{{\rm obs},i}$ is the observing bandwidth used at ith epoch and f_d is the filling fraction of the number of scintles, for which we assume a moderate value of 0.5. The measurement error on the above three quantities is estimated as

$$\sigma_{{\rm meas},g} = [(\sigma_{{\rm mod},g})^2 + (\sigma_{{\rm est},g})^2]^{0.5}\ . \tag{A2}$$

The errors obtained in this manner are given in columns (3) and (4) of Table 5 for $v_{d,g}$ and $\tau_{d,g}$, respectively. Typical values range from 2%–5%, with somewhat larger values for PSRs B1237+25 and B1929+10, for which $\sigma_{{\rm meas},g} \sim 10\%$.

The measurement error in the flux density, $\sigma_{{\rm meas},F}$, is estimated as

$$\sigma_{{\rm meas},F} = \left[\left(\frac{1}{N_{\rm ep}} \right)^2 \left(\sum_{i=1}^{i=N_{\rm ep}} \{\sigma_{F,i}\}^2 \right) \right]^{0.5}, \tag{A3}$$

where $\sigma_{F,i}$ is the measurement error in flux density at ith epoch, and it includes the errors due to calibration ($\sigma_{\rm cal}$) and estimation error ($\sigma_{\rm est}$) due to the finite number of scintles at that epoch. We have adopted a conservative approach of 10% uncertainty in calibration for all the epochs. Column (5) of Table 5 gives $\sigma_{{\rm meas},F}$, typical values of which range from 2%–5%, except for PSRs B1237+25 and B1929+10, for which $\sigma_{{\rm meas},F} \sim$ 8%–9%.

A direct estimation of the statistical error is not possible, because our time series are not good enough to estimate the timescale of fluctuations of the quantities. However, we get a first-order estimate based on the expected refractive timescale ($\tau_{\rm ref}$), which can be estimated from measurements of decorrelation bandwidth and scintillation timescale. We estimate the statistical uncertainty as

$$\sigma_{\rm stat} = \left(\frac{x_{\rm rms}}{\sqrt{N_{\rm ref}}} \right), \tag{A4}$$

where $x_{\rm rms}$ denotes the rms estimate of the quantity x under consideration and obtained from the time series. A rough estimate of the number of refractive cycles of fluctuations ($N_{\rm ref}$) is given by $T_{\rm sp}/\tau_{\rm ref}$, where $T_{\rm sp}$ is the time span of observation. The refractive timescale is taken as $\tau_{\rm ref} \approx u^2 \tau_d$ (Rickett 1990). We use values of $v_{d,g}$ and $\tau_{d,g}$ to get estimates of $\tau_{\rm ref}$. The errors computed in this manner are given in columns (6), (7), and (8) of Table 5, for $\langle v_d \rangle$, $\langle \tau_d \rangle$, and $\langle F \rangle$, respectively. Typical values lie in the range of 5%–15% for $\langle v_d \rangle$, 3%–10% for $\langle \tau_d \rangle$, and 5%–20% for $\langle F \rangle$.

REFERENCES

Armstrong, J. W., Rickett, B. J., & Spangler, S. R. 1995, ApJ, 443, 209
Bhat, N. D. R., Gupta, Y., & Rao, A. P. 1997, in Lecture Notes in Physics 506, The Local Bubble and Beyond, ed. D. Breitschwerdt, M. J. Freyberg, & J. Trümper (Berlin: Springer), 211
———. 1998, ApJ, 500, 262
Blandford, R. D., & Narayan, R. 1985, MNRAS, 213, 591
Bondi, M., Padrielli, L., Gregorini, L., Mantovani, F., Shapirovskaya, N., & Spangler, S. R. 1994, A&A, 287, 390
Cognard, I., Bourgois, G., Lestrade, J., Biraud, F., Aubry, D., Darchy, B., & Drouhin, J. 1993, Nature, 366, 320
Cole, T.W., Hesse, H. K., & Page, C. G. 1970, Nature, 225, 712
Cordes, J. M. 1986, ApJ, 311, 183
Cordes, J. M., Pidwerbetsky, A., & Lovelace, R. V. E. 1986, ApJ, 310, 737
Cordes, J. M., & Rickett, B. J. 1998, ApJ, 507, 846
Cordes, J. M., Weisberg, J. M., & Boriakoff, V. 1985, ApJ, 288, 221
Cordes, J. M., & Wolszczan, A. 1986, ApJ, 307, L27

Fiedler, R. L., Dennison, B., Johnston, K. J., & Hewish, A. 1987, Nature, 326, 675
Fiedler, R. L., et al. 1994, ApJ, 430, 581
Gould, D. M. 1994, Ph.D. thesis, Univ. Manchester
Gupta, Y. 1995, ApJ, 451, 717
Gupta, Y., Rickett, B. J., & Coles, W. A. 1993, ApJ, 403, 183
Gupta, Y., Rickett, B. J., & Lyne, A. G. 1994, MNRAS, 269, 1035
Gwinn, C. R., Taylor, J. H., Weisberg, J. M., & Rawlings, L. A. 1986, AJ, 91, 338
Hewish, A. 1980, MNRAS, 192, 799
Hewish, A., Wolszczan, A., & Graham, D. A. 1985, MNRAS, 213, 167
Huguenin, G. R., Taylor, J. H., & Helfand, D. J. 1973, ApJ, 181, L139
Kaspi, V. M., & Stinebring, D. R. 1992, ApJ, 392, 530
LaBrecque, D. R., Rankin, J. M., & Cordes, J. M. 1994, AJ, 108, 1854
Lestrade, J., Cognard, I., & Biraud, F. 1995, in ASP Conf. Ser. 72, Millisecond Pulsars: A Decade of Surprise, ed. A. Fruchter, M. Tavani, & D. Backer (San Francisco: ASP), 357
Lestrade, J., Rickett, B. J., & Cognard, I. 1998, A&A, 334, 1068
Lyne, A. G., & Smith, F. G. 1982, Nature, 298, 825
Narayan, R. 1988, in AIP Conf. Proc. 174, Radiowave Scattering in the Interstellar Medium, ed. J. M. Cordes, B. J. Rickett, & D. C. Backer (New York: AIP), 17
Rickett, B. J. 1969, Nature, 221, 158
———. 1977, ARA&A, 15, 479
———. 1986, ApJ, 307, 564
———. 1990, ARA&A, 28, 561
Rickett, B. J., Coles, W. A., & Bourgois G. 1984, A&A, 134, 390
Roberts, J. A., & Ables, J. G. 1982, MNRAS, 201, 1119
Romani, R. W., Narayan, R., & Blandford, R. D. 1986, MNRAS, 220, 19
Scheuer, P. A. G. 1968, Nature, 218, 920
Selvanayagam, A. J., Praveenkumar, A., Nandagopal, D., & Veluswamy, T. 1993, IETE Tech. Rev., 10, 333
Sieber, W. 1982, A&A, 113, 311
Smith, F. G., & Wright, N. C. 1985, MNRAS, 214, 97
Spangler, S. R. 1988, in AIP Conf. Proc. 174, Radiowave Scattering in the Interstellar Medium, ed. J. M. Cordes, B. J. Rickett, & D. C. Backer (New York: AIP), 32
Stinebring, D. R., & Condon, J. J. 1990, ApJ, 352, 207
Stinebring, D. R., Faison, M. D., & McKinnon, M. M. 1996, ApJ, 460, 460
Subramanian, R. 1989, Ph.D. thesis, Indian Inst. Sci.
Swarup, G., et al. 1971, Nature Phys. Sci., 230, 185
Taylor, J. H., & Cordes, J. M. 1993, ApJ, 411, 674
Taylor, J. H., Manchester, R. N., & Lyne, A. G. 1993, ApJS, 88, 529
Wolszczan, A., & Cordes, J. M. 1987, ApJ, 320, L35